# A detailed view into the eruption clouds of Santiaguito volcano, Guatemala, using Doppler radar

L. Scharff,[1] F. Ziemen,[1,2] M. Hort,[1] A. Gerst,[1,3] and J. B. Johnson[4]

Received 25 May 2011; revised 13 February 2012; accepted 16 February 2012; published 5 April 2012.

[1] Using Doppler radar technology we are able to show that eruptions at Santiaguito volcano, Guatemala, are comprised of multiple explosive degassing pulses occurring at a frequency of 0.2 to 0.3 Hz. The Doppler radar system was installed about 2.7 km away from the active dome on the top of Santa Maria volcano. During four days of continuous measurement 157 eruptive events were recorded. The Doppler radar data reveals a vertical uplift of the dome surface of about 50 cm immediately prior to a first degassing pulse. Particle velocities range from 10 to 15 m/s (in the line of sight of the radar). In 80% of the observed eruptions a second degassing pulse emanates from the dome with significantly higher particle velocities (20–25 m/s again line of sight) and increased echo power, which implies an increase in mass flux. We carry out numerical experiments of ballistic particle transport and calculate corresponding synthetic radar signals. These calculations show that the observations are consistent with a pulsed release of material from the dome of Santiaguito volcano.

**Citation:** Scharff, L., F. Ziemen, M. Hort, A. Gerst, and J. B. Johnson (2012), A detailed view into the eruption clouds of Santiaguito volcano, Guatemala, using Doppler radar, *J. Geophys. Res.*, *117*, B04201, doi:10.1029/2011JB008542.

## 1. Introduction

[2] Dome growth and explosive degassing are fundamental processes in continental arc volcanism. Both processes occur at various magnitudes from slow magma plug extrusion to hazardous dome collapse events that release gas and ash several km high into the atmosphere, produce block and ash flows, or pyroclastic flows. The activity at dome growing volcanoes can be characterized as vulcanian, sub-plinian, or plinian. Their explosive degassing events are highly complex but the infrequency of events, compared to for example Strombolian [e.g., *Harris and Ripepe*, 2007] or Hawaiian [*Heliker and Mattox*, 2003] eruptions, still hinders detailed in situ studies of their eruption dynamics. The fundamental processes of dome growth as a consequence of magma degassing and crystallization, thereby increasing its viscosity, have been modeled in various studies [e.g., *Voight and Elsworth*, 2000; *Hale and Wadge*, 2003; *Barmin et al.*, 2002; *Melnik and Sparks*, 2005; *de Michieli Vitturi et al.*, 2008; *Taisne and Jaupart*, 2008; *Massol and Jaupart*, 2009] as well as the buoyant ascent of (sub-)plinian eruption columns [e.g., *Wilson et al.*, 1978; *Sparks et al.*, 1997; *Oberhuber et al.*, 1998; *Esposti Ongaro et al.*, 2007]. The dynamics of volatiles and ash particles directly at the vent during vulcanian-type explosive degassing events, however, is subject to ongoing research — mainly because a quantitative observation of these processes is rather difficult.

[3] Unfortunately most dome building volcanoes (e.g. Merapi, Colima) are not as accessible as volcanoes exhibiting Strombolian activity in terms of installing multiparameter networks and actually visually observing dome activity. In this regard the Santa Maria volcano complex, Guatemala, and its since 1922 growing child volcano Santiaguito are a "unique observation site" [*Bluth and Rose*, 2004] to study vulcanian eruption processes directly at the vent. Standing on top of Santa Maria volcano (3772 m asl) allows to directly view down the 100 year old horseshoe shaped scar onto Santiaguito volcano (~2550 m asl) and its currently active dome named Caliente (see Figure 1).

[4] Surface degassing at Santiaguito has been subject of several studies based on infrasonic and thermal data [e.g., *Johnson et al.*, 2004; *Sahetapy-Engel et al.*, 2004; *Patrick et al.*, 2007; *Sahetapy-Engel and Harris*, 2009; *Marchetti et al.*, 2009] as well as using a $SO_2$ camera [*Holland et al.*, 2011]. Like plinian eruptions, vulcanian degassing events comprise a jet transporting a mixture of ash and gas. Once ejected, the hot particle-gas mixture entrains ambient air, eventually becomes buoyant and, following the terminology of *Patrick* [2007a], *thermals* or *rooted thermals* develop. In contrast to plinian eruptions, vulcanian explosions are orders of magnitude smaller. If there is a gas jet at all at Santiaguito volcano, the transition from jet to buoyant regime occurs about 50 m above the vent [*Sahetapy-Engel and Harris*, 2009]. *Sahetapy-Engel and Harris* [2009] further find that the plume height does not depend on exit velocity,

[1]Klimacampus, Institut für Geophysik, Universität Hamburg, Hamburg, Germany.
[2]Now at Max-Planck-Institute for Meteorology, Hamburg, Germany.
[3]Now at European Astronaut Centre, European Space Agency, Cologne, Germany.
[4]Department of Earth and Environmental Science, New Mexico Institute of Mining and Technology, Socorro, New Mexico, USA.


0148-0227/12/2011JB008542

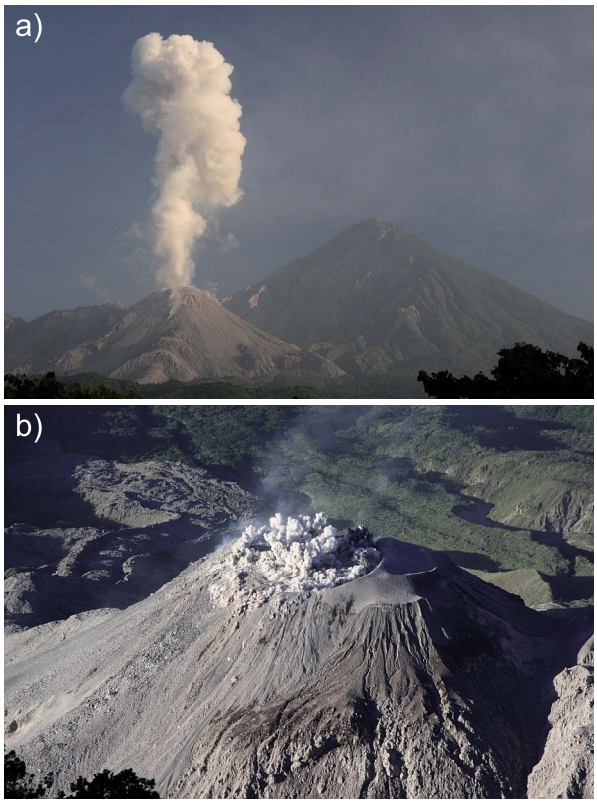


**Figure 1.** (a) View from south toward Santiaguito volcano, which is located inside the collapse structure of the south-western wall of Santa Maria volcano. (b) Onset of an eruption at Santiaguito volcano as viewed from the top of Santa Maria volcano (view toward south-west), where the Doppler radar was set up.

but instead on buoyant ascent velocities, lateral spreading rates and feeder plume radii. Determining the exit velocity using the plume front velocity near the vent during the first second of an eruption, *Sahetapy-Engel and Harris* [2009] find that the higher the total heat budget of the ascending plume, the higher is its buoyant ascent velocity.

[5] Thermal imaging via camera or other sensors allows to estimate the velocity of the hot plume front by tracking isotherms. However, this is biased by rapid cooling of the plume front (due to e.g. entrainment of ambient air, adiabatic expansion, and condensation of juvenile and ambient moisture). In addition the plume front velocity does neither represent the gas' nor the particles' velocity. The dynamics at the source feeding the plume may be observed by tracking individual particles. Here one has to discriminate between large particles (>1 m) that can be detected from a safe distance with a regular camera and small particles (<10 cm) that are undetectable with this technique. Unfortunately, larger particles, which are inertially driven, often move decoupled from the plume on ballistic trajectories so that information on the small (mm-sized) particles is required to study the plume dynamics. In addition, the internal dynamics of a plume cannot be observed by a camera as they are obscured by the outer part of the plume, and the relationship between velocities in the inner core and the outer edge of the plume is unknown [*Patrick*, 2007a].

[6] The Doppler radar provides highly accurate velocities of small-to-large particles and an estimate of the evolution of the mass flux, which allows us to reconstruct in detail the dynamics at the onset and during an explosive degassing event. We first summarize the multidisciplinary experiment and describe the data collected during the experiment. This is followed by a modeling section to calculate ballistic particle trajectories and corresponding synthetic Doppler radar spectra. Afterwards we compare synthetic and measured data to draw conclusions on the eruption dynamics at Santiaguito volcano and discuss our results.

## 2. Multidisciplinary Experiment at Santiaguito Volcano

[7] In order to investigate the links between magmatic degassing and the dynamics of volcanic eruptions we participated in a multidisciplinary experiment at Santiaguito volcano, Guatemala that took place between January 3rd and 14th, 2007. During this experiment several different instruments (seismometers, University of North Carolina; infrasound sensors and a high-resolution video camera, University of New Hampshire; Doppler radar, Hamburg University; infrared camera, Universidad de Colima) were deployed. The seismic and infrasound loggers were provided by PASSCAL (Program for Array Studies of the Continental Lithosphere, New Mexico Tech). More information on the setup, location and recording dates are given by *Johnson et al.* [2008]. The Doppler radar was positioned near the top of Santa Maria volcano at 3600 m asl pointing downward at the active dome Caliente of Santiaguito volcano (2550 m asl, inclination 27°, see Figure 2). Also installed on top of Santa Maria were an acoustic sensor as well as a thermal and a high-resolution video camera. The Doppler radar operated from Jan. 9, 17:30 UTC to Jan. 13, 17:30 UTC and recorded 157 eruptive/explosive events. More details on the general aspects of the experiment can be found in the work of *Johnson et al.* [2008]. Here we focus on the interpretation of the Doppler radar data.

### 2.1. Activity of Santiaguito Volcano

[8] Santiaguito's activity is mainly characterized by extrusive activity of silicate-rich lava flows and vulcanian explosions. In January 2007 vulcanian explosions occurred about every 90 min and emanated from a ring-shaped distribution of fractures on the dome center and circumference (Figure 1b), which has been suggested to be related to the geometry of the conduit [e.g., *Bluth and Rose*, 2004]. *Gonnermann and Manga* [2003] argue that the highest shear stresses in a non-Newtonian channel flow are located at the conduit walls. These high shear stresses may cause magma fragmentation and thereby lead to a ring-shaped arrangement of vents. This interpretation would imply a nearly cylindrical conduit that is blocked by a lava plug. However, *Johnson et al.* [2008] believe that these fractures are simply failure joints in the brittle lava flow carapace rather than persistent features. Explosions produced white and gray plumes that sometimes rose up to 4000 m above sea level.

### 2.2. The Doppler Radar

[9] Doppler radar instruments transmit electromagnetic waves (wavelength between 3 m and 3 mm) that are reflected

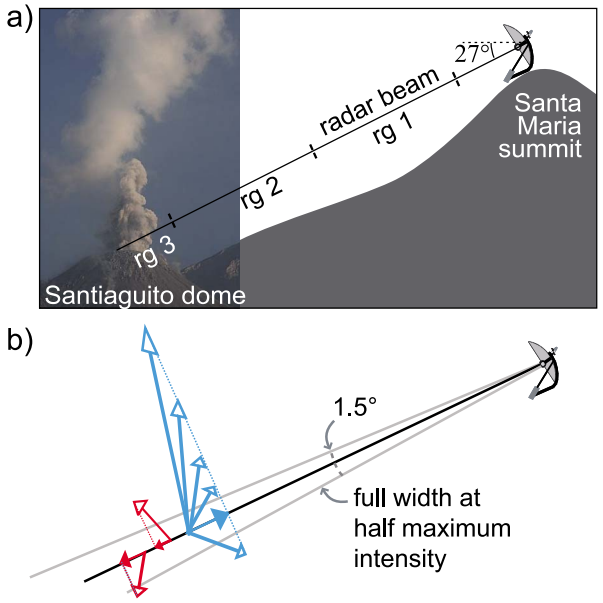


**Figure 2.** (a) Setup geometry of the Doppler radar instrument near the summit of Santa Maria (view from south-east). The tick marks on the radar beam show the range resolution of the chosen radar setup, here 1000 m. (b) Also shown is the relationship between measured (filled arrows) and true velocities (open arrows). The blue arrows (filled) indicate a positive radial velocity whereas red arrows (filled) represent negative radial velocities. Note that particles with different velocities may have the same radial velocity. Especially negative velocities may resemble falling as well as rising particles, but due to the geometry of this measurement and the mainly vertically ejected particles, we can assign negative velocities to falling particles. The black line marks the center of the radar beam (maximum intensity) and the gray lines show the beam opening (not to scale).

back to the instrument by a stationary or moving object (here volcanic ash). The reflected signal differs in frequency from the transmitted signal by a frequency shift (Doppler effect) that is proportional to the radial velocity of the particle (radial meaning the velocity component parallel to the radar beam, i.e. toward or away from the instrument). Two main Doppler radar designs have been established: pulsed and continuous wave (CW) systems. Our instrument is a frequency modulated continuous wave (FM-CW) radar, which can be deployed almost everywhere in the field due to its low weight (50 kg) and low power consumption (40W, both values include the data logger). It operates at a frequency of 24 GHz (wavelength of $\lambda$ = 1.25 cm) and transmits a power of 50 mW. The radar beam has a total aperture of 1.5° and the intensity of the transmitted energy inside the beam largely follows a Gaussian distribution [e.g., *Hort et al.*, 2003, Figure 5]. In addition to the velocity measurement, the frequency modulation of our instrument allows us to determine the approximate distance of the moving object by subdividing the distance along the beam into so-called range gates [*Barrick*, 1973].

[10] Each particle inside the radar beam reflects a distinct amount of energy that depends on the particle's size, shape, and composition [*Adams et al.*, 1996]. Particles with sizes on the order of the wavelength (here $\lambda$ = 1.25 cm) have a very complex reflection pattern, which can be calculated using Mie theory [*Mie*, 1908]. Very small particles ($r \leq \lambda/10$) and larger particles ($r > 10\lambda$) are within the range of Rayleigh scattering and geometrical optics, respectively. As a zero-order approximation we can assume that bigger particles reflect more of the electro-magnetic wave than smaller particles. Our small wavelength allows us to detect particles of e.g. 1 mm radius at a distance of 2.6 km when a minimum concentration of 2.66 g/m$^3$ is exceeded (distributed homogeneously in probed volume). During a given time interval the Doppler radar records the reflected energy at discrete frequency shifts, i.e. discrete velocities (so-called bins). This means that the observed reflected energy for a certain velocity range is the sum of the reflected energy of all particles moving at different velocities within this range. The resulting output is a velocity spectrum, showing for each range gate, how much reflected energy is attributed to each velocity.

[11] During the Santiaguito experiment the temporal resolution of our instrument was near 20 Hz, the velocity resolution was 0.39 m/s. Particles moving toward the radar show by definition positive velocities, whereas particles that move away from the radar have negative velocities. The maximum unambiguous radial velocity was ±49.92 m/s, which was never exceeded during our measurements. The large distance of 2.7 km led to a range gate length of 1000 m to record the signal in the third range gate (2500–3500 m along beam). At the target distance, the field of view (FOV) has an approximate diameter of 70 m (cross-beam, full width at half maximum of Gaussian intensity distribution). The illuminated area on the dome surface is an ellipse of 8500 m$^2$. For more technical aspects on our Doppler radar the reader is referred to *Vöge and Hort* [2009]. For the use of pulsed Doppler radar systems in volcanology see *Dubosclard et al.* [1999] or *Gouhier and Donnadieu* [2008].

### 2.3. Data Processing and Presentation

[12] Evaluating eruption characteristics requires the definition of some scalar values that can be used to characterize each spectrum. Each radar spectrum consists of discrete values: Each velocity $v_i$ is associated with a certain amount of reflected energy $P_i$, where $i$ = 1, .., $n$ and $n$ being the number of discrete velocity bins. From each spectrum we determine the maximum positive ($V^+_{\max}$) and negative ($V^-_{\max}$) radial velocity and sum the reflected energy of the positive and negative velocity range [*Hort et al.*, 2003]:

$$P^+ = \sum_{i=1}^{i_{V^+_{\max}}} P_i, \qquad P^- = \sum_{i=-1}^{i_{V^-_{\max}}} P_i. \tag{1}$$

The resulting values $P^+$ and $P^-$ are referred to as echo power and will be used as a proxy for the mass moving inside the considered range gate. Those definitions are similar to the ones used by *Dubosclard et al.* [2004]. With the measurement setup at Santiaguito volcano, where the radar is tilted 27° downward and the assumption that the particles' initial velocities are mainly directed in the vertical direction,

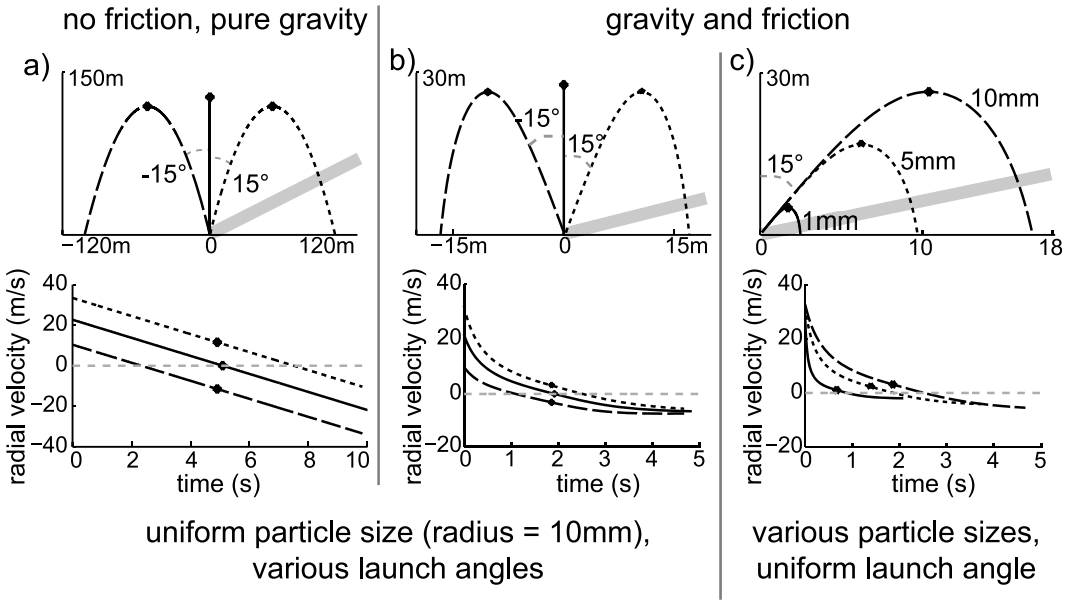


**Figure 3.** Simple examples of ballistic particle transport in non-moving air and their time lines of radial velocity (pseudo velocigram) as it would be measured with the Doppler radar. The top diagrams show the particle trajectories. In these examples particle transport is confined to the image plane. All particles are initialized with an absolute velocity of 50 m/s. The gray bar represents the radar beam direction. The lower diagrams show the pseudo velocigram, i.e. the particles radial velocity as a function of time. Note that in a pseudo velocigram the echo power of all particles is assumed constant and equal to unity. The horizontal gray dotted line marks the zero velocity. A particle's trajectory and the corresponding pseudo velocigram are coded using the same line style. The apex of the particles trajectories is marked with a black dot in space (top diagrams) and time (bottom diagrams). (a and b) The effect of the launch angle on the radial velocities. All particles have a radius of 1 cm. In Figure 3a friction with air is neglected and only gravity acts on the particles, hence particle motion is independent of their size and acceleration is constant. Friction leads to a size-dependent terminal fall velocity as can be seen in Figures 3b and 3c. (c) The effect of particle size on velocity. Here all particles have the same launch angle (15° toward the radar). Their radii are 1 mm, 5 mm, and 1 cm. For more explanation see text.

positive radial velocities can be attributed to rising particles (see Figure 2b). The same argument leads to the assignment of negative radial velocities to falling or settling particles. In the following we refer to radial velocities as velocities otherwise we will explicitly give the direction (e.g. vertical velocity).

[13] In addition to the values of maximum velocities and echo power, we plot the complete Doppler radar information in a so-called velocigram [see also *Gerst*, 2010]. An example of a velocigram is shown in Figure 5, where the data is introduced. In a velocigram, each point holds the information on echo power (color) corresponding to a certain velocity (y-value) at a particular time (x-value). The colors represent the ratio of reflected energy to background noise in dB (dark blue is background noise):

$$P_i^{dB} = 10 \log_{10} \frac{P_i}{P_{\text{noise}}}. \quad (2)$$

The value for background noise $P_{\text{noise}}$ is a constant that is arbitrarily chosen for each experiment. The conversion of reflected energy to echo power in dB is done to eliminate the calibration constant, which contains antenna gain and internal system properties. Note that the echo power can not be converted to the usually given radar reflectivity Z, which is only applicable when the particle diameter is small compared to the wavelength.

### 2.4. A Simple Example and the Impact of the Measurement Geometry

[14] As explained above, the radar only measures the radial velocity component of objects along the radar beam (see Figure 2b), hence we measure a 1D velocity profile through the 3D processes occurring during an eruption. To enhance the readers' understanding of the recorded radar data we briefly discuss a simple eruption geometry and how it is seen by the radar using a synthetic model.

[15] The simplest scenario in terms of an explosive event at a volcano is the ballistic transport of various particles ejected from a vent that represents a point source. In Figure 3 we plot the trajectories and corresponding pseudo velocigrams for three particles moving through still air with neglecting friction (Figure 3a) and applying friction (Figure 3b) with air as described in Appendix A. Pseudo velocigram means in this case that the velocity component parallel to the radar beam (beam inclination is 27° to the horizontal) is plotted as a function of time, but the value of reflected energy is constant and equal for all particles at all times. This is equivalent to the assumption that the illumination of the particles is always the same. All particles have the same radius (1 cm) and an initial

velocity of 50 m/s. The only difference is the launch angle. One particle is launched vertically and the others are launched at an angle of ±15° to the vertical. All three trajectories lie in a plane that is defined by the radar beam, i.e. those examples are calculated in 2D. Consider a particle that is ejected vertically. Neglecting friction with air (Figure 3a), this particle is only subject to gravity, which leads to a constant acceleration toward the ground. Ejecting particles on inclined trajectories shifts the recorded velocity toward positive or negative velocities by a constant that solely depends on the x-component of the initial velocity.

[16] Introducing friction with air (see Appendix A for a full description of friction and trajectory calculation) the trajectories of the three particles change (Figure 3b). The vertically ejected particle's radial velocity representation in the velocigram is a curved line that bends toward a maximum falling velocity. The friction force acts in the direction opposite to velocity, gravity only influences the vertical velocity component. Hence the velocigrams of the sub-vertically ejected particles also follow curved lines and, because the horizontal velocity component decreases, the difference in radial velocity between the three particles decreases and those curved lines converge to the same settling velocity. This velocity is the terminal fall velocity.

[17] The dependency of terminal fall velocity on particle size can clearly be seen in Figure 3c). To illustrate the effect of different particle sizes on the velocity evolution, we show trajectories and pseudo velocigrams for three particles with 1 mm, 5 mm, and 1 cm radius. All particles are launched with 50 m/s at an angle of 15° to the vertical, toward the radar. Apparently, small particles (<5 mm) are more affected by friction. The larger a particle, the less curved is its velocigram representation and the higher is its terminal fall velocity.

[18] The geometry of the instrument setup, i.e. non-vertical incident angle of the radar beam, has a major effect on the measured velocities. Using a vertical incidence Doppler radar, the assignment of positive radial velocities to rising particles (and negative to falling, respectively) is obvious because the horizontal velocity component is perpendicular to the radar beam and therefore not detected. This is also the main reason why a radar looking vertically upward is a very precise rain rate measurement [*Löffler-Mang et al.*, 1999]. In the above examples, however, we used a radar beam inclination of 27° to the horizontal, which is similar to the measurement setup at Santiaguito volcano. Therefore the horizontal velocity component greatly influences the measured velocity and the above assignment of positive and negative velocities is only a first-order approximation. In Figure 3 the transition from rising to falling (i.e. the apex of the trajectory) is marked in all diagrams. Particles on inclined trajectories obviously deviate from the assignment near their apex due to their significant horizontal velocity component. For bigger particles, which are less influenced by friction, the erroneously assigned positive velocity while already falling significantly differs from the true velocity. Particles that are departing from the radar might be even measured with a negative velocity during their entire risetime, given that their launch angle is larger than 27° to the vertical and away from the radar.

[19] In the above examples, however, we only show pseudo velocigrams and neglect that the reflected energy depends on the number of particles, their position inside the radar beam and, in addition, on the particle radii. Particles might leave the field of view near their apex and hence their "false" radial velocity is not seen by the radar. The measured radial velocity also depends on the particles position inside the beam, because only the component in direction of the radar is measured. I.e. the angular distance of a particle at the beam edge (i.e. where the intensity decreased to 50%) and the radar beam direction is 0.75°. Due to our relatively narrow beam opening angle, those varying directions (27° ± 0.75°) can be neglected.

[20] In the simple examples particles are erupted into a non-moving atmosphere, i.e. there is no wind. At a volcano however, the air certainly moves and influences particle movement. Air motion is due to various contributors: e.g. background wind, volatile expansion and jetting, turbulent entrainment of ambient air, and hence buoyant updraft. Every single component leaves a trace in the velocigram, which is more or less characteristic. A wind that is parallel to the radar beam for example adds a constant velocity to the particle velocity (neglecting particle inertia) and hence shifts the whole measured velocity to higher or lower velocities, depending on the overall direction of the wind (positive for wind toward the radar, negative otherwise). A wind perpendicular to the beam blows particles out of, or into the field of view. Furthermore, gas expansion and jetting are very complex processes. Their main effect is the transport of small particles to greater heights, which means, that those particles need longer to fall down. Buoyant updraft acts in the vertical direction and hinders particles from falling. In fact, it further expands the coda as particles might be even floating in the upwind. For a more detailed analysis of the influence of those environmental parameters on ballistic transport and resulting Doppler radar data, the reader is referred to Appendix B and the auxiliary material.[1]

## 3. Characteristics of Eruptions

[21] For identifying events in our data set we use an automatic event detection algorithm, where the echo power $P^+$ (see equation (1)) is used as an indicator for volcanic activity. This basic event detection has been successfully applied to data from Stromboli [*Scharff et al.*, 2007] and Merapi [*Vöge and Hort*, 2008a, 2008b]. A total of 157 events has been detected, 120 of which show a good signal-to-noise ratio and were selected for analysis. In January 2007, events at Santiaguito volcano were randomly distributed over time and show no characteristic event duration: Events last from 10 s (weak single pulse) to 120 s (see Figure 6c) and on average the event duration was about 30 s.

[22] At line-of-sight distance of 2.7 km the field of view (FOV) of the Doppler radar, projected on the dome surface, is an ellipse with a diameter of about 144 m (along beam, long axis) and 70 m (across, short axis). The radar beam intensity decreases to 50% at 40 m height above the target location (beam center hitting surface). Because the dome is ~200 m wide, we changed the target location of the radar beam during the experiment (see Figure 4) in order to observe different parts of the dome. Of the 120 eruptions evaluated, 34 were observed at beam target location C (center of incandescence), 5 at IR (inner ring), 73 at OR

[1] Auxiliary materials are available in the HTML. doi:10.1029/2011JB008542.

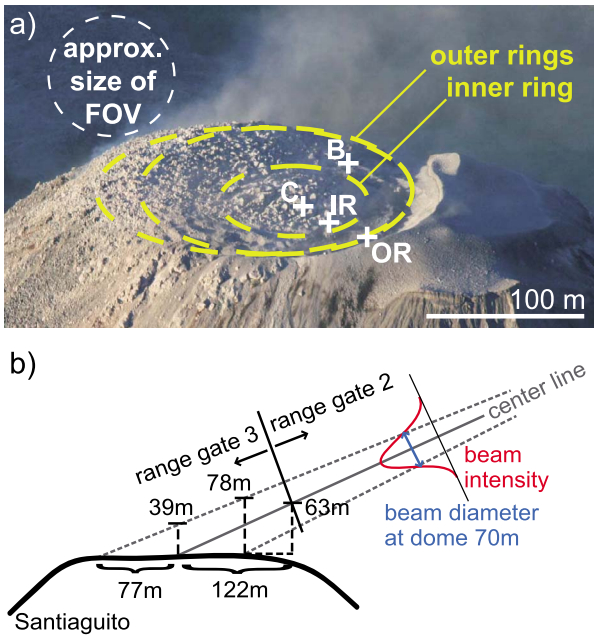


**Figure 4.** (a) Beam target locations (white crosses) and approximate size of field of view (FOV) as seen from the radar location. Every cross marks the respective center of the FOV, whose footprint on the dome surface is also circular from this perspective. Yellow lines show the approximate location of inner and outer rings, the source of the explosive activity, in January 2007. Note that at beam target location OR a significant amount of the FOV is filled by the supposedly non-moving flank, whereas at location B a portion of the beam passes above the dome surface. (b) Schematic drawing of the measurement geometry viewed perpendicular to the beam (from left in Figure 4a). On the dome surface, the FOV footprint is elliptical and has a radius of 77 m (long axis) and 35 m (short axis). The radar beam edges (equal to the half maximum beam intensity) are indicated by gray dotted lines and their heights above the dome surface are given. In this study we focus on the processes directly at the vent and hence limit the data interpretation to range gate 3 (2500–3500 m slant distance). The beam crosses the dome surface at about 2640 m slant distance from the radar.

(outer ring), and 8 at location B (back side). All data shown here was recorded in range gate 3 (see Figure 4b), i.e. show the lowermost 80 m of the eruption.

[23] In Figures 5 and 6 we show the data of 5 example eruptive events recorded at 4 different beam target locations (see Figure 4). Each diagram shows a velocigram and the amount of reflected energy (calculated using equation (1)) as a function of time. For one of the events we show high-resolution video still images at 4 selected points in time. Directly at the onset of this event (white arrow in Figure 6b) there is no visible degassing carrying ash. In the second image, a first ash cloud can be spotted near the dome center, after which the activity shifts to the outer ring at the circumference of the dome (see Figure 6e). Interestingly, in some parts of the dome surface no fractures develop and the surface stays intact. After another 5 s into the eruption several ash-loaded plumes — preferentially at the outer rings — obscure the view onto the less ashy dynamics inside the eruption cloud(s) and the processes on the dome surface. *Patrick* [2007b] states that the gas mass fraction at Santiaguito is very high (>0.3), in which case we can assume that the radar beam penetrates the whole plume hence providing an integrated overview over particle velocities.

[24] The Doppler radar data have two important features, which we interpret. Most of the eruptive events show a strong echo power at the lowest resolvable velocity (+0.39 m/s radial, see white arrows in Figures 5a, 5b, 6a, and 6b) that occurs 1–2 s before particles with higher velocities are detected. This strong signal at $P_1$ (echo power corresponding to $v_1 = 0.39$ m/s) lasts 0.5 to 1 s and there is no significant amount of reflected energy at any higher velocity during this time. Interestingly, the intensity and appearance of this feature depends on the beam target location (see Figure 4a): It is clearly visible in 82% of the C

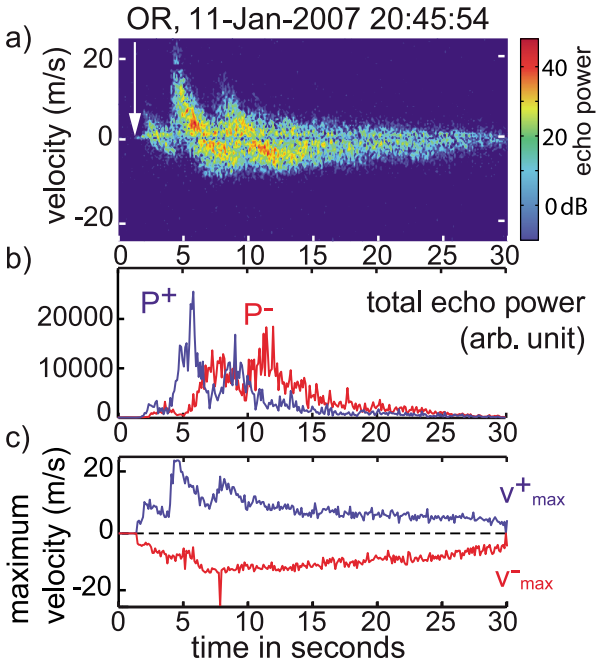


**Figure 5.** Data set of one eruptive event recorded in range gate 3 (2500–3500 m slant distance) at beam target location OR (see Figure 4a). (a) Velocigram showing the echo power (color coded) as a function of velocity (y-axis) and time (x-axis). Note that the colors represent the ratio of echo power and background noise in dB, meaning dark blue (=0 dB) is background noise. This representation of the Doppler radar data gives an overview on an entire eruptive event and clearly shows periods of high and low activity. Note that the apparent gap at 18 m/s results from the removal of an interfering signal, which does not affect the quality of the data. The white arrow marks the onset of the eruptive event as detected by the radar. (b) The amount of reflected energy as a function of time, calculated from equation (1). The blue line refers to the total energy reflected by particles having a positive velocity, the red one to negative velocities, respectively. (c) The maximum radial velocity as a function of time. The blue line refers to the positive maximum radial velocity, the red one to the negative maximum radial velocity, respectively. Note that the lines of maximum velocity are essentially the envelope of the signal shown in the velocigram (transition from dark to light blue).

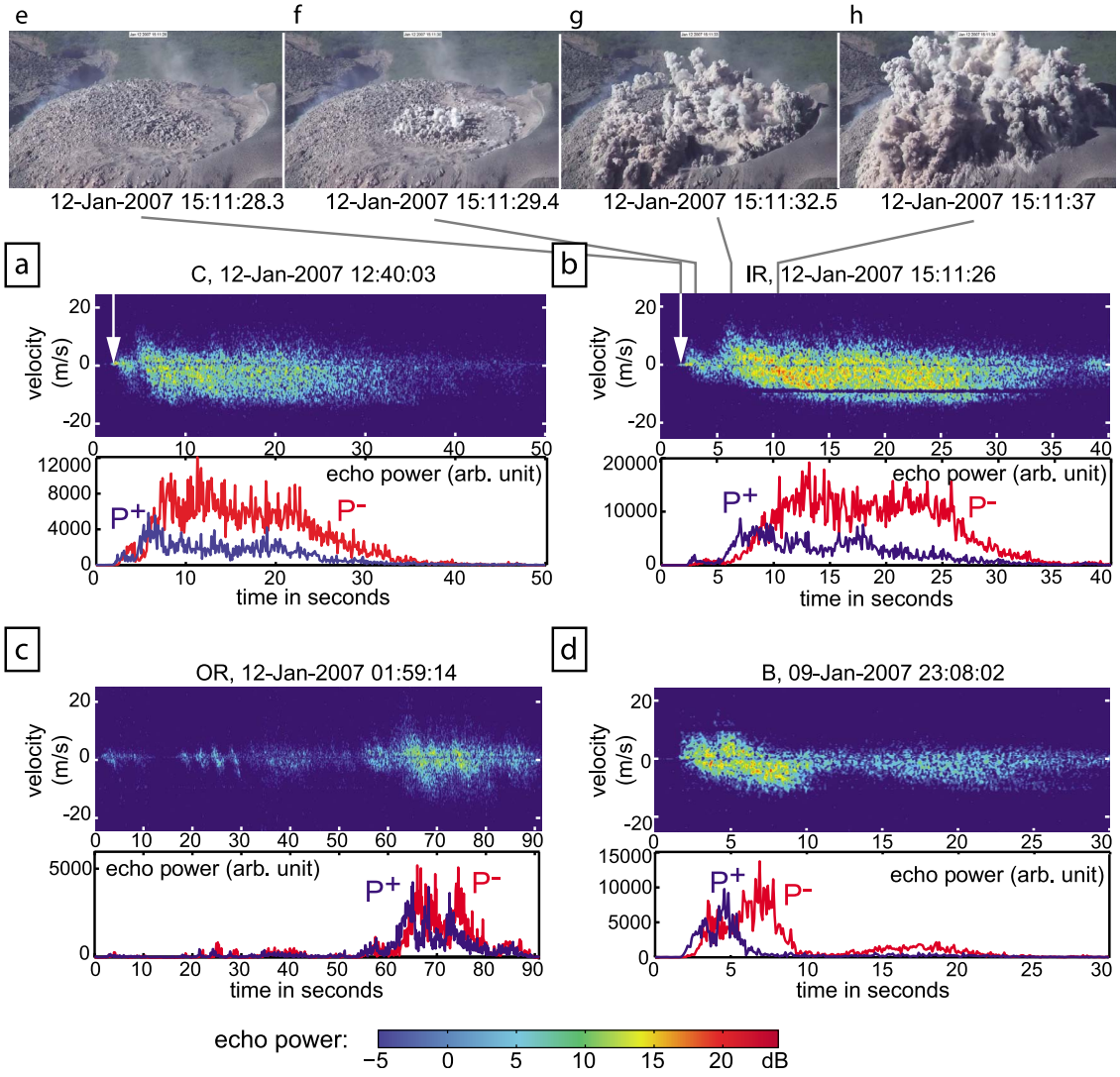


**Figure 6.** (a–d) Data sets of four eruptive events recorded at different beam target locations (see Figure 4a) and (e–h) video still images of eruptive event B. For each of the four events we show the velocigram (top) and the total reflected energy for positive and negative velocities (bottom). See Figure 5 for an explanation of the radar data. High-resolution images show the dome surface directly before dome uplift (Figure 6e), the first pulse in the center (Figure 6f), the second pulse at the outer ring (Figure 6g), and chaotic plumes afterwards (Figure 6h). The respective point in time in the velocigram of event B is marked by the gray lines. The apparent gap in event B at −8 m/s results from the removal of an interfering signal which does not affect the quality of the data.

($P_1 \approx$ 16–19 dB) and IR ($P_1 \approx$ 16–17 dB) targeting events, whereas we found this signal in only 64% of the events recorded at OR ($P_1 \approx$ 15 dB). In half of the location B targeting events we do not observe this signal at all and in the other events, it is only very weak ($P_1 \approx$ 12 dB). Note that $P_1$ values lie between 5 and 10 during the eruption, independent of the beam target location.

[25] The second feature is a fluctuating eruption intensity throughout an eruption (Figures 5 and 6), which can be seen in all 5 velocigrams (top of each panel). These fluctuations have a dominant period of 3–5 s and last for 3–12 s. They start with an increased echo power at high positive velocities, i.e. a sudden increase in maximum velocity, which is followed by a decrease in velocity. The maximum echo power eventually passes the zero velocity axis and the negative maximum velocity increases. During an eruption the echo power of rising ($P^+$) and settling ($P^-$) particles shows some local maxima, herein also termed pulse (for a precise definition of pulse see section 4.2). However, identifying individual pulses is more conspicuous using additional information from the temporal evolution of the velocities, which is summarized in the velocigram. Independent of the beam target location, 83% of all events show two or more pulses.

[26] In addition to these two main features, (1) strong signal at the lowest resolvable positive velocity and (2) pulses, 40% of the pulsed events show additional characteristics: (3) an

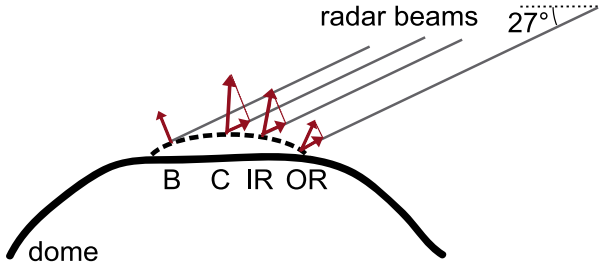


**Figure 7.** Schematic drawing of the uplift of the dome (view from south-east, same as in Figure 2). Four beam target locations are marked and their corresponding radar beams are shown in gray. The uplift velocity and the corresponding radial velocity are given with red arrows for each beam target location. Because the distance of radar and beam target location is much bigger than the distance between the beam target locations, the radar beam angle can be considered as constant.

increasing intensity in echo power from 1st to 2nd pulse and (4) a higher maximum velocity for the 2nd pulse (Figure 5 and Figures 6a, 6b, and 6d). In contrast, Figure 6c shows a long lasting stable sequence of very weak pulses. Almost all of the multiple pulsed events show an increasing intensity (in terms of maximum velocity as well as in terms of echo power) from the first to the second pulse. While this increase is small or non-existent for pulses observed at locations B and C, we find a significant increase in both maximum velocity and echo power for the first two pulses at the rings (locations OR, 30% of events, and IR, all events, see Figure 4). At OR and IR, velocities increase from 10–15 m/s to 15–25 m/s and total echo power from below $10^3$ to $10^4$ and more. At the same time the duration of single pulses increases from ~3 s to more than 5 s.

[27] Sequences of very weak pulses (Figure 6c) are only visible at the OR-location (see Figure 4) and account for 12% of OR targeting events. These 1–2 min long series of pulses with echo power around 10 dB are always followed by a few stronger pulses (higher velocities and more echo power). The weak pulses occur nearly every 3 s (or multiples of 3 s) and last about 2 s. The reflected energy for rising and settling particles is of the same order, and maximum positive and maximum negative radial velocities are equal.

## 4. Data Interpretation

### 4.1. Low-Velocity Peak at Eruption Onset

[28] In section 3 we mentioned a strong signal at the lowest resolvable velocity (+0.39 m/s, radial toward the radar), which appears up to a second before the onset of the explosive event. Interestingly, this low-velocity peak is almost not visible at location B on the far side of the dome (see Figure 6d), where we recorded a total of 8 events. Except for observations targeted at location B, 81% of all other events show this signal (see white arrows in Figure 5 and Figures 6a and 6b).

[29] To be able to interpret this signal we have to take a more in depth look into the processing of the signal in the radar. Consider a particle that is moving at a velocity $v_p = v_i + \alpha\, dv$, between two velocity samples ($v_i$ and $v_i + dv$, $0 < \alpha < 1$). The echo power of that particle is only distributed to those two velocity samples with respect to $\alpha$. There is no contribution to any higher or lower velocity sample. The echo power of a very slow moving particle ($v_p < +0.39$ m/s) will hence be distributed between 0 m/s and the smallest velocity sample located at $v_1 = +0.39$ m/s. However, for data processing reasons the echo power at 0 m/s is being filtered out by a comb notch filter and cannot be used to deduce the particle's true velocity by comparing neighboring velocity samples. Because the signal appears at $v_1 = +0.39$ m/s but not at $v_2 = +0.78$ m/s we can assume that the true velocity measured here is less or equal +0.39 m/s (along beam).

[30] The echo power value $P_1$ at $v_1 = +0.39$ m/s can be interpreted as the weighted integral over all reflecting surfaces that are moving with velocities between 0 and +0.39 m/s in the FOV toward the radar. The weighting factors depend on the lateral distance of the reflector from the radar beam center and the size and true velocity of the reflector. A strong signal at $v_1 = +0.39$ m/s without any signal at negative velocities before or afterwards could therefore be caused by (1) a volume with a high concentration of particles near the radar beam center that suddenly moves at less than +0.39 m/s and disappearing after 0.5 s or (2) the dome surface accelerating to a velocity of less than +0.39 m/s and stopping again after 0.5 s. We favor the latter explanation because (1) no ash could be observed on the high-resolution videos at corresponding times [see *Johnson et al.*, 2008, online supplement], (2) velocities are too slow to transport enough ash particles into the radar beam to explain the strong signal, (3) no negative velocities could be observed, hence no particles fall down directly before or after the strong signal, (4) the signal is almost similar for beam target locations C, IR, and OR, thus independent of the location of possible vent centers, (5) wind cannot explain the regular appearance 1.5 s before the explosion, and finally (6) the radial velocity component of a bulging dome surface would appear similar at beam target locations C, IR, and OR, but should be less detectable at location B (see Figure 7). This is consistent with our data: 81% of the events at locations C, IR, and OR show this distinct signal but no event recorded at location B shows this precursor.

[31] We assume the observed low-velocity peak is caused by a non-uniform uplift of the dome surface (see Figure 7). The illuminated dome surface is largest at target location C and IR. At location B and OR a large fraction of the radar beam passes the dome surface or illuminates the flank, which leads to smaller echo power values at $P_1$ at those locations. At OR, however, the non-uniform uplift causes an almost 'along beam'-motion of the surface, which increases the echo power value of $P_1$ compared to location B, where motion is almost perpendicular to the radar beam (i.e. zero radial velocity, see Figure 7). The FOV at beam target location B also comprises a part of the FOV when targeting C, but due to the Gaussian intensity distribution of the radar beam, those contributions to the echo power are small.

[32] Using particle image velocimetry (PIV), *Johnson et al.* [2008] found that large sections of the dome's surface are lifted 20–50 cm at eruption onset. Our data supports this finding. In addition, since the signals duration is ~0.5 s we calculate a radial uplift of 20 cm (44 cm vertical) which is in a very good agreement with *Johnson et al.* [2008], who obtained up to 0.5 m of vertical uplift.

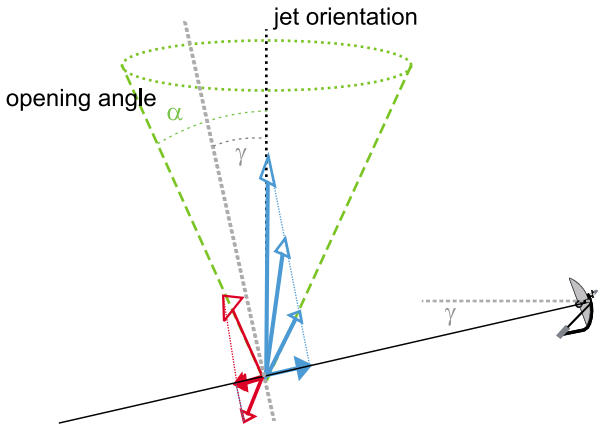


**Figure 8.** Geometry of initial velocities, opening angle ($\alpha$) and radar beam inclination ($\gamma = 27°$). Arrows indicate velocity vectors of particles, vector length mirrors particle speed. Filled arrows show the radial velocity component as measured by the radar. Blue vectors show examples with a positive radial velocity, red vectors show negative velocity examples. Due to the 1D measurement we cannot distinguish between rising and falling particles that have the same velocity component into the direction of the radar beam. However, the velocity evolution over time can be used to separate the contribution of rising and falling particles to the echo power. The absence of negative radial velocities at the beginning of the eruption underlines that $\alpha < \gamma$ at Santiaguito volcano.

### 4.2. Fluctuating Echo Power

[33] As explained above, the echo power is related to the size of the reflecting surface. During the eruption, when ash is ejected with gas, this surface is the cumulative backscatter cross section of all ash particles inside the probed volume. The backscatter cross section (or radar cross section, RCS) of a particle is related to its optical cross section, the relation being highly complex and non-linear. As a first order approximation, however, we can assume that the bigger a particle, the more it reflects (see also section 5.4).

[34] The absolute amount of material moving through the beam cannot be calculated from the reflected energy, because the particle size distribution of the erupted material is unknown. However, the relative change in echo power does reflect changes in mass flux assuming the particle size distribution does not change dramatically from one eruption to another [for details on this see *Hort et al.*, 2006].

[35] Every pulse in echo power starts with the sudden increase in echo power at high positive velocities, hence a sudden increase in maximum velocity. The maximum positive velocity decreases directly after reaching its maximum value at the beginning of a pulse. The total echo power $P^+$ increases in conjunction with the sudden velocity jump, but is less steep, which leads to the assumption that the particles are ejected over a longer time span during one pulse. After reaching its maximum, $P^+$ decreases again with almost the same rate as it increased before. At the same time $P^-$ increases. This means that the particles of different size reach their individual apexes one after another (see also discussion of Figure 3).

[36] Interestingly, the maximum in $P^+$ always coincides with a minimum in $P^-$ and vice versa. The sum of total echo power in the range gate ($P^+ + P^-$) is almost constant after the second pulse, i.e. the volume of moving particles does not change dramatically. The maxima in $P^+$ (and also $P^-$) occur with a period of 3–5 s, which is similar to the time span a particle travels on its ballistic trajectory (see Figure 3). The staggering of $P^+$ and $P^-$ peaks can be explained for example by a wind (i.e. some turbulent gas motion) that forces a fixed volume of particles to move alternately up and down. The draw back of this explanation is the acceleration phase, when the wind direction shifts from down to up. We do not observe a slow increase in positive maximum velocity as would be required here. Another explanation is that the pulses are independent of each other and the volume flux into the FOV is constant and balances the volume flux out of the FOV (e.g. due to ash sedimentation).

[37] The geometry of the measurement is such that we observe particles that exit the vent. Hence a sudden jump in maximum velocity and direct decrease afterwards means that particles enter the FOV with their highest velocity, i.e. they are accelerated to their respective maximum velocity either below the dome surface or somewhere else outside the FOV and behave like ballistic objects once they entered the FOV (compare to Figure 3). Therefore every pulse (characterized by a sudden jump in maximum velocity in conjunction with an increase in total echo power $P^+$) is independent of the other pulses in an eruption. The term pulse therefore refers to the sudden release of (maybe overpressurized) gas that percolated through cracks in the conduit fill thereby accidentally entraining ash particles and accelerating them by air drag to their size dependent terminal settling velocity (relative to the gas jet velocity). The velocity observed by the radar is the radial component of the particles true velocity. This means that depending on the angle between radar beam and particle trajectory the measured radial velocity is always less than the particles true velocity (or equal at zero angle). Hence the maximum radial velocity is the minimum approximation for the velocity of the fastest particle and hence for the gas velocity, which we assume to be moving vertically. Therefore we use the maximum radial velocity converted to a vertical velocity to approximate the gas velocity of 20–35 m/s for the first pulse and 35–60 m/s for the second and later pulses.

[38] Given that at the beginning of a pulse (at least for the first and second) no particles with negative velocities are observed, we can constrain the geometry of the pulse (see Figure 8). High-resolution videos [see *Johnson et al.*, 2008, online supplement], recorded from the location of the radar, indicate that at the onset of an eruption particle trajectories are not perfectly vertical but show a certain opening angle. For certain events the opening angle is observed to be bigger for the first pulse emanating from the center of the dome (±20–30°) than for the second pulse at the outer ring (±10–20°). This is in agreement with the radar data from which we can deduce that the opening angle of all eruptions must be smaller than 27°: Assuming that no particles fall down at the onset of a pulse, a negative radial velocity would correspond to particles that move at an inclination larger than 27° with respect to the vertical (red vectors in Figure 8), which we do not observe.

[39] Within the first pulse the echo power of rising particles is almost equal to that of settling particles, whereas during the second pulse the energy reflected by the settling particles is often up to two times larger, which can be explained by

(1) radar beam attenuation, (2) the measurement setup and (3) wind. The attenuation of the radar beam depends on the concentration of scatterers due to shadowing effects and multiple scattering. This means that the same particle volume returns less echo power when it is concentrated near the beam axis than evenly distributed in the probed volume. In an eruption, the bulk density of the erupting gas-particle mixture is presumable highest at the pulse onset and decreases as the particles decouple from the gas and spread out. Second, the probed volume atop the dome surface can be completely filled by falling particles, independent of the beam target location. Rising particles, however, are constrained to the volume of a top-down cone directly above the vent with an opening angle of less than the beam inclination (see Figure 8). Due to the distribution of vents, the FOV only covers a few of them and hence only a small fraction of the rising particles is observed. The falling particles may be blown into the FOV from vents outside the FOV. A third explanation is based on a background wind that blows away from the radar, so that the measured radial velocities are all shifted toward negative velocities (for more details on this see Appendix B and Figure B2). The difference between first ($P^- \approx P^+$) and secondary pulses ($P^- \approx 2P^+$) can not be explained solely by wind. It is rather an indication of the number and position of active vents: Equal echo power in positive and negative velocities means that everything that passed the FOV on its way up falls down through the FOV again. This is true for example, when assuming a single active vent somewhere inside the FOV and a narrow opening angle. When more falling as rising particles are observed, additional vents outside the FOV are active. This leads to the assumption that the first pulse preferentially emanates from a vent near the dome center and secondary pulses occur at vents at the outer rings. This finding is supported by the high-resolution videos [see *Johnson et al.*, 2008, online supplement], where first activity can be spotted near the center before it spreads out to the dome circumference.

## 5. Simulating Doppler Radar Data

[40] The radar was aiming at different target locations on the dome (see Figure 4), which allows us to explore temporal as well as spatial characteristics of the ring eruptions. Because only one radar was deployed, we observed one eruption at one location at a time and therefore cannot interpret all details in a quasi 3D analysis. However, we were able to identify major characteristics for each beam target location (see section 4.2) and constrained parameters describing the 'standard eruption' at Santiaguito. In this section we use our numerical model to further strengthen the hypothesis that events at Santiaguito volcano are composed of a series of single explosive pulses of varying intensity and location, and to explore the influence of the beam target location on the measured data.

[41] Before turning to the model results we note that unlike other studies [*Marzano et al.*, 2006; *Gouhier and Donnadieu*, 2008] we do not attempt to match the actual amount of echo power by adjusting the particle size distribution (PSD). As has been shown by *Ziemen* [2008] it is impossible to extract the particle size distribution as well as the total mass of particles from a single radar measurement without further assumptions. Any attempt to determine the actual mass of particles being erupted requires prescribing a distinct PSD. Hence the masses calculated in the following cannot be viewed as the true total mass but instead is a relative mass that depends exclusively on the assumed PSD.

### 5.1. The Numerical Model

[42] The results shown here are produced using a numerical model to calculate ballistic particle transport and corresponding synthetic radar spectra. A complete description including all equations is given in Appendix A). For the dynamic part we use a Lagrangian formulation of ballistic particle transport in air. Following *Herzog et al.* [1998] atmospheric friction (atmospheric drag) is calculated for both Newtonian and Stokian friction for each particle and the higher of both values is applied to the particle. That means fast particles are subject to Newtonian friction whereas slow particles undergo Stokian friction. The gas thrust phase (jet) is parameterized through an upward wind, whose velocity depends on the radial distance to the center of the eruption column. This implementation of the atmosphere is similar to the model developed by *Dubosclard et al.* [2004] and *Gouhier and Donnadieu* [2008].

[43] Crater and vent geometry as well as initial conditions like particle size distribution (PSD), gas velocity, and opening angle are free parameters of the model. It has been shown in previous studies that the PSD is well described by a Weibull distribution [*Weibull*, 1951; *Marzano et al.*, 2006] (see also Figure 9). Vent conditions may change with time during an eruptive event. Therefore the PSD and maximum launch velocity of particles are allowed to vary with time. Following *Chouet et al.* [1974] we assume the particle launch velocity $|v_{p0}|$ to depend on the particle radius $r$

$$\left|v_{p0}(r,t)\right| = w_{g0}(t) - \sqrt{\frac{8g\rho_s}{3c_w\rho_g}r}, \tag{3}$$

where $c_W = 1$ is the empirically determined drag coefficient for ash [*Pfeiffer et al.*, 2005]. $\rho_g$ and $\rho_s$ are the density of gas and solids and $g$ is gravity. $w_{g0}(t)$ is equal to the gas jet velocity and varies with time according to a prescribed function (constant, increasing or decreasing). Gas jet velocity and particle size distribution can be configured for arbitrary time periods. Hence, we can build complex scenarios of vent near conditions for which we calculate synthetic radar spectra.

[44] Once particle size, location, and velocity of the particles are determined from the ballistic part of the model described above, we calculate the amount of energy reflected by each particle as a function of time. We include geometric spreading but neglect atmospheric absorption, multiple scattering, and interference. The synthetic radar beam has an opening angle of 1.5° with the intensity inside the beam following a Gaussian distribution.

[45] Scattering of electromagnetic waves at ash particles is calculated using Mie theory [*Mie*, 1908]. In brief, Mie describes the interplay of a particle's internal and external electro-magnetic fields. In the Mie region, the external field wavelength and the particle size are of the same order of magnitude (see Figure 9a). Here a so-called creeping wave [*Currie*, 1989] travels around the particle interfering constructively or destructively, hence the amount of back-scattered

energy strongly depends on the ratio of particle size and wavelength. In one end-member case, when the wavelength of the external field is small compared to the particle size, the internal field will almost match the external field and the particle's back-scattering cross section is almost equal to its geometric (or optical) cross section. In the Rayleigh region (the other end-member), when the particle is very small compared to the wavelength, the energy is scattered almost isotropically in all directions, hence only a very small fraction is scattered back toward the radar. Because we assume that size and dielectric properties do not change significantly over time, the back-scatter cross sections need to be calculated only once for each particle size. This is done by an external program in advance.

### 5.2. Initial Conditions

[46] Here we try to fit the 'shape' and 'trends' of the event shown in Figure 5 as it comprises three clearly visible pulses. The vent positions are fixed and not changed to reach a 'best fit'. The vent releasing the first pulse is located near the dome center at position C (see Figure 4), while the second and third pulse are set to several vents that are positioned on a circle of diameter 200 m around the dome center (representing the outer ring). Figure 10 shows the vent positions and measurement setup as well as the initial conditions derived from observations discussed above.

[47] Particle directions are randomly distributed inside the opening angle (±25° here) around a directivity axis, which for simplicity is assumed to be vertical for all pulses. A more precisely constrained opening angle would require a 3D measurement using three radar systems, as has been successfully demonstrated by *Vöge et al.* [2005] and *Gerst et al.* [2008].

[48] In summary, the modeled eruption consists of three pulses: a first pulse with a gas velocity of 35 m/s at a vent near the dome center, followed by two pulses from the vents located at the ring. The second and third pulse have a higher gas velocity (60 m/s). We observe an almost linear decay in maximum velocity. According to Figure 3 particles with radii >5 mm are mainly affected by gravity and their velocity also decays almost linearly, where smaller particles (<1 mm) move with the gas. The big particles however are ejected with slower velocities due to their size and hence cannot be responsible for the almost linear decay in maximum velocity. We therefore assume that the gas jet velocity decays linearly.

[49] The geometry of the example eruption was chosen to be similar to the setup of our instrument at Santiaguito, i.e. the distance to the vent is 2.6 km and the inclination of the radar beam is 27° (see Figure 4b). The PSD is assumed to be the same for all pulses (see black lines in Figures 9b–9d), but the volume flux for the first pulse is half of the volume flux of later pulses where the volume is spread over the distributed vents (see Figure 10b). We assume a linear decay in volume flux to account for the possible explosive nature of ash release. To show how the same event is seen by the radar

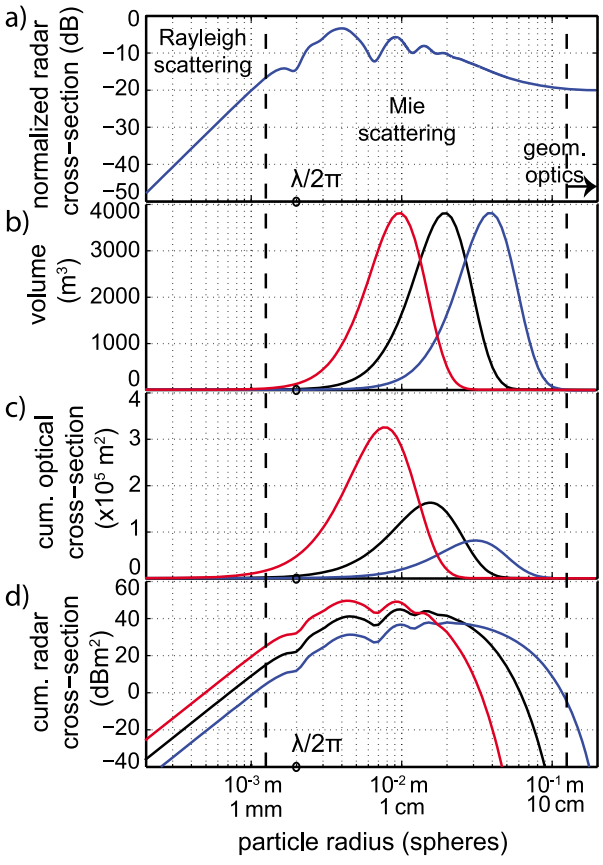


**Figure 9.** Radar cross section (RCS) and particle size distributions (PSD) used in the model calculations presented here. (a) Normalized radar cross section (or back-scatter cross section, dB) of a single particle normalized to its optical cross section. RCS is calculated for a wavelength of $\lambda$ = 1.25 cm and using the complex refractive index of ash at high frequency $\epsilon = 2.458 + 0.02197i$ [*Adams et al.*, 1996]. RCS is a function of particle radius and wavelength. When $r < 0.1\lambda$ the normalized RCS increases proportional to $r^4$ (Rayleigh scattering). In the other direction, when $r > 10\lambda$ the normalized RCS increases proportional to the optical cross section. In the region where $0.1\lambda < r < 10\lambda$, a so-called creeping wave travels around the conducting sphere interfering constructively or destructively (Mie scattering). That is, using our 24 GHz-Doppler radar (wavelength $\lambda$ = 1.25 cm) a 4 mm-sized particle reflects five times more energy per unit area than a 6 mm-sized particle. (b) The PSDs follow a Weibull distribution and differ only in the mean particle radius, 5 mm (red lines), 10 mm (black lines), and 20 mm (blue lines). Minimum radius (0.6 mm), maximum radius (40 mm) and shape parameter of the Weibull distribution (1.5) are held constant. Note that using a shape parameter of 1.5, the radius corresponding to the maximum in volume is twice, whereas the radius corresponding to the maximum number of particles (mode of the PSD) is approximately half of the mean radius of the distribution. (c) Cumulative optical cross section of all particles in the PSD. This view represents the area that is covered when all particles are spread out. Because the total volume is constant, the cumulative optical cross section is smaller for PSDs with higher mean particles sizes. (d) The cumulative radar cross section ($dBm^2$) is the summed RCS of all evenly sized particles in the PSD. Note that we use the black PSD (10 mm mean radius) in all model calculations unless stated otherwise.

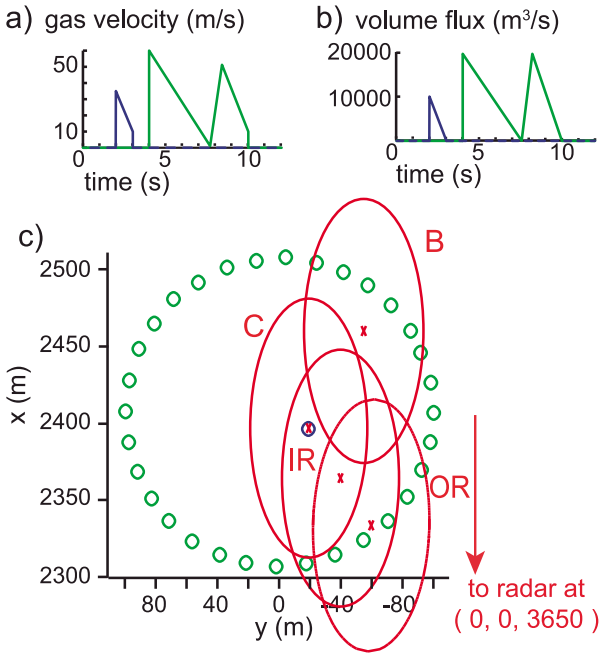


**Figure 10.** Initial conditions for the model calculations of the temporal evolution of the eruption. (a) Evolution of maximum launch velocity over time. The launch velocity can be interpreted as initial gas velocity and is related to the particles launch velocity via the particles terminal fall velocity (see equation (3)). The colors relate the velocity to the respective active vent. (b) Assumed volume flux for the modeled eruption. The colors represent the vent(s) to which the volume flux is evenly distributed. (c) Top view of the simulated dome surface (at z = 2550 m) with its vent distribution. The first active vent is located near the center (blue circle). The very special ring-type eruptions of Santiaguito are modeled using a ring of radius 100 m consisting of 32 evenly spaced vents (green circles). We assume a constant vent diameter of 10 m. Red ellipses show the four different FOVs (from top to bottom: B, C, IR, and OR). The radar position is at coordinates (x = 0 m, y = 0 m, z = 3650 m) and indicated with the red arrow. The PSD used in our model calculations is given in Figure 9, input parameters for atmosphere and radar configuration are: $\rho_g$ = 0.897 kg/m$^3$ at $T$ = 300 K, $R_{air}$ = 287 J/kg/K, $u$ = 1.82 × 10$^{-5}$ Pa s, $c_W$ = 1.0, $z_{\mathrm{ref}}$ = 50 m (gas jet reference height), range gate length = 1000 m, $v_{Ny}$ = 49.92 m/s (maximum unambiguous velocity), $dv$ = 0.39 m/s and output is calculated for range gate 3 (2500–3500 m).

from different beam target locations, we calculate the synthetic data for all 4 beam target locations.

[50] Although the atmosphere is rarely at rest at a volcano, we neglect any background wind in our calculations to keep the model simple. We also do not account for entrainment of ambient air and buoyant updraft of the developing ash cloud as the radar is aiming at the source region of an eruption, which is dominated by the gas thrust so that buoyant rise and entrainment have little effect on the dynamics. The transition of an inertia driven gas jet to buoyantly driven plume rise is at Santiaguito slightly below 50 m height above the dome surface [*Sahetapy-Engel and Harris*, 2009]. Because the probed volume extends to ~40 m height above the beam center and the beam intensity is maximum near the dome surface (i.e. the vents), we neglect buoyant updraft in our model calculations. The effect of buoyancy on particle motion is shown in Appendix B. Main effects are (1) an overall shift of echo power toward positive velocities since particles terminal velocities are relative to the surrounding gas velocity and (2) a long coda of slowly falling and floating particles.

[51] *Patrick* [2007a] observed at ash-rich Strombolian eruptions (Type 2a) that a vigorous entrainment vortex at the plume front could only develop after reaching fully buoyant behavior (i.e. above our FOV). The entrainment needed to reach the buoyant phase is due to small scale turbulent shearing along the edges of the jet [*Suzuki et al.*, 2005; *Patrick*, 2007a]. Although the main mechanism that produces the gas jet differs (bubble bursting in the conduit at Stromboli versus gas flow through an interconnected network of fractures in dome surface at Santiaguito), the ash gets entrained incidentally by the gas flowing through a layer of ash [*Patrick*, 2007a, 2007b] (see backfilling material at Stromboli or covering the dome surface at Santiaguito). Once the gas-ash-mixture left the vent, the processes in the plume, which are investigated here, are independent of the conduit processes. How a vortex ring displays in a pseudo velocigram is given in the auxiliary material. Note that small scale turbulence is also neglected. Turbulence is often simulated as adding a small random velocity vector to the particle's velocity in every time step. The overall motion (diagonal bended streak due to gravity and air friction, see Figure 3) will be superposed by random velocity deviations, but still dominate the velocigram. This means that sharp lines in a velocigram will become smeared across neighboring velocities in real data where turbulence is important.

### 5.3. Model Results

[52] In Figure 11 the real data and synthetic velocigrams are shown for the different radar beam target locations C, IR, OR, and B calculated from the ballistic model. The detailed motion of the particles is shown in three animations which are part of the auxiliary material. In each animation the particles are colored, highlighting a different variable (particle radius, beam intensity for beam target location OR and echo power for beam target position OR). Within their first 10–15 m of rise particles bigger than 1 mm (radius) decouple from the gas jet and eventually fall back to the ground (negative velocities, see Animation S1). The mm-sized particles rise with the gas and start settling when the gas jet faded. Hence small particles accumulate during the course of an eruption.

[53] The overall shape (maximum velocities) and trends in $P^+$ and $P^-$ for the real data (Figure 11a) do fit those of the modeled eruption presented in Figure 11e). As explained above, we did not try to fit the absolute values for echo power (arbitrary units). Importantly, the maximum velocities observed at the different locations on the dome are nearly the same, in agreement with the radar data, but the reflected energy of these signals varies significantly. For example, if we take the initial pulse (see first second in temporal evolution) that originates at the center of the plume, the amplitude of the reflected signal is highest at the location C, which is directly targeting this location. This pulse is hardly visible when the

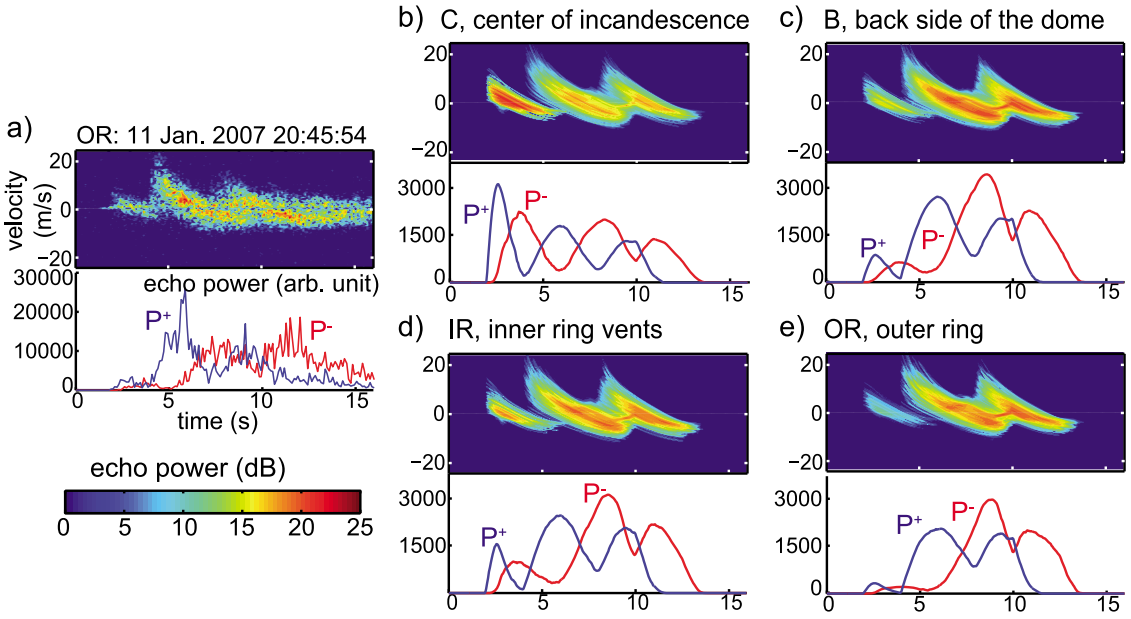


**Figure 11.** (a) Real data and (b–e) synthetic data sets of one eruptive event, observed for different beam target locations. For a short description of displayed values see Figure 5. The first pulse is most obvious in C and IR, whereas the echo power of outer ring pulses is higher in OR and B (see also Figure 10). The model parameters (vent conditions, PSD and eruption geometry were chosen to result in a best fit. The best fit criterion is the similarity of velocigrams in Figures 11a and 11e in maximum velocity and total echo power trend. For further discussion see text.

beam is aiming at location OR, where only a small fraction of the transmitted energy is reflected by erupted material (see Animations S2 and S3). This is because the radar beam has an opening angle of 1.5° and the intensity inside the beam follows a Gaussian distribution (see Figure 10).

[54] All velocigrams have alternating peaks in $P^+$ and $P^-$. They show a slow increase in $P^+$ (compared to the jump in maximum velocity). After reaching its maximum $P^+$ decreases at almost the same rate as it increased before and $P^-$ increases. Hence assuming a pulsed volume flux seems to fit our data. Nevertheless contrary to the real data, the summed echo power ($P^+ + P^-$) increases slightly in the synthetic data sets (after the second pulse). Hence the true volume flux seems to decrease with eruption duration as more and more particles accumulate in the FOV.

[55] The maximum velocity at pulse onset in the synthetic velocigrams equals those in the real data set (Figure 11a), which justifies our simple assumption to use the maximum radial velocity converted to a vertical velocity as gas jet velocity. However, the decay in the synthetic data differs from the almost linear decay in Figure 11a, which indicates that during the pulse the maximum radial velocity underestimates the true gas jet velocity.

### 5.4. The Particle Size Distribution

[56] The particle size distribution (PSD) is a badly constrained parameter since no published PSD exists for Santiaguito. We have tested different PSD (different mean grain sizes) and find a good agreement with the radar data using the PSD shown in Figures 9b–9d (black line, 10 mm). Grain sizes at Santiaguito are smaller than at for example Stromboli [see *Marchetti et al.*, 2009] due to the different fragmentation mechanism. We assume that the PSD does not change significantly from one event to the other and especially not during one event.

[57] While exploring the effect of single parameters, we found that the main parameter controlling total echo power is the total erupted volume. The more particles move inside the radar beam, the higher the echo power. A smaller effect can be achieved by changing the range of particle sizes to smaller or bigger at constant eruptive volume, but this effect is not linear (see below and Figure 9). In our model the PSD controls the echo power of particles and their initial velocities. When we increase the gas velocity, for example, we also have to increase the minimum particle size to give the same maximum initial velocity. To get the same echo power values as with the slower gas velocity, we also have to increase the total volume of the PSD (to keep the cumulative radar cross section constant). Therefore we can reproduce a single velocity spectrum with a large number of different PSDs. Initial velocity and size of a particle, however, affect its ballistic motion due to the size-dependent drag force. Hence using consecutive spectra constrain the PSD. We can therefore deduce from the evolution of maximum velocity and total echo power if our assumed PSD is correct within an order of magnitude.

[58] The range of particles sizes used here is kept constant and is chosen due to the following reasons: the minimum particle size that can be calculated by our model (numerically stable using a time step of 0.01 s) is 0.6 mm, which is already in the Rayleigh scattering region (see Figure 9a). Hence the radar cross section of even smaller particles diminishes with the sixth power of their radius and can be neglected. Second, the maximum particle size is constrained by the gas jet velocity. We use equation (3) to assign an initial velocity to the particle. Hence, only particles whose

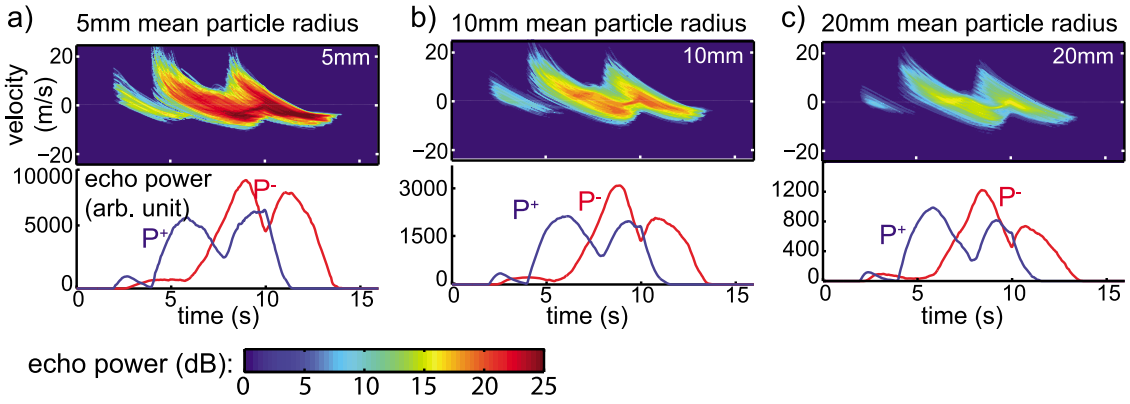


**Figure 12.** The same eruptive event (see Figure 11) observed at OR using different particle size distributions (PSD). The range of particles and the total volume is constant, but the mean particle radius is varied from (a) 5 mm, (b) 10 mm to (c) 20 mm. Note that Figure 12b is the same velocigram as shown in Figure 11e. The PSDs are given in Figure 9. The synthetic velocigrams for the other beam target locations are given in the auxiliary material.

radius satisfies $r > 1/2(w_{g0}/k)^2$ exit the vent and therefore particles $r > 4$–5 cm can be neglected here.

[59] In Figure 12 we show the same model calculation as in Figure 11e with a smaller (Figure 12a) and a larger (Figure 12c) mean particle size. The corresponding PSDs are given in Figures 9b–9d. The most prominent effect of changing the mean grain size at constant total volume is that the cumulative optical cross section for increasing mean particle radius decreases. Hence also the echo power is less for a larger mean grain size. In addition, the normalized radar cross section of mm-sized particles is bigger than that of the cm-sized (see Figure 9a), which means they reflect more energy per unit area than the big particles.

## 6. Discussion and Conclusive Remarks

[60] In this paper we have demonstrated how Doppler radar observations can be used to shed new light on the dynamics of Santiaguito volcano, Guatemala. Our observations reveal that the eruptions at Santiaguito volcano are composed of several single pulses about once every 3–5 s during an event.

[61] Most of the 157 events recorded during the experiment with the Doppler radar were pulsed eruptions with several single explosions during one eruptive event (85% for locations C and IR and 49% for locations B and OR). Video footage shows that the eruptions often begin at the center of the dome and then move to the outer rings. Using a single radar we were not able to resolve this change in eruption location during a single event. Instead we targeted different locations of the dome and see clear evidence that the center as well as the outer rings are involved. The first pulse is different from the following ones: it has a slower maximum velocity and less echo power. In addition, $v^+_{max} \approx |v^-_{max}|$ indicates that the first pulse is almost not influenced by any wind and comprises mainly ballistically flying particles that are subvertically ejected. The total echo power depends on the beam target location, which indicates that every FOV illuminates the active vent(s) of the first pulse, but with different intensity. On the contrary, the echo power of secondary pulses is almost the same at every beam target location. Hence every FOV comprises several active vents, but maybe different ones. There is almost no difference between the second and following pulses, which in turn suggests that those later pulses originate also at the outer rings, which cannot be seen in the videos.

[62] The short wavelength of our instrument (1.25 cm) enables us to simultaneously detect small buoyantly rising as well as larger particles that move ballistically. Hence we collected 1D measurements through processes that are inherently 3D, which complicates data evaluation. Therefore we make use of numerical modeling of particle transport during explosive degassing at multiple locations and calculate the corresponding radar spectra.

[63] Synthetic velocigrams (see Figure 11) and real data sets (see Figure 6) both show similar features. Repeated sudden increase in positive maximum velocity, followed by a slow increase in negative maximum velocity and alternating peaks in echo power of rising and settling particles can for example be explained by repeated degassing pulses.

[64] The retrieval of synthetic spectra is based on a simple ballistic model, where the particle's initial velocity is related to its size. Using equation (3) we assume that all particles have been accelerated in a conduit by the ejecting gas and that all particles have reached their terminal fall velocity relative to the gas [*Steinberg and Babenko*, 1978]. In other words, the particle velocity is equal to the gas velocity minus terminal settling velocity. In nature particles will reach their terminal velocity only at open conduit systems with conduits wide and long enough and without internal obstructions, and assuming that the particle concentration inside the conduit does not influence the two-phase flow itself. At Santiaguito, however, gas erupts through small cracks and fractures of the dome surface, hence the above conditions are not exactly satisfied.

[65] Our approximation of the gas exit velocity using the maximum radial velocity converted to a vertical velocity tends to overestimate the true gas velocity. The maximum radial velocity most probably belongs to a particle that is not moving vertical [*Gouhier and Donnadieu*, 2011]. Assuming

all particles have the same absolute velocity the maximum radial velocity belongs to the most inclined particle and the gas velocity is overestimated by a factor of 1.7, which is the ratio of particle velocities on a vertical and the most inclined trajectory (27° toward the radar) that result in the same radial velocity. Nevertheless, this definition of the initial particle velocity provides a simple scaling between each particle's size and velocity that has the advantage of being intuitive but tends to overestimate the true exit velocity as it marks the upper limit for the gas and particle velocities. Furthermore we only interpret the temporal evolution of maximum velocities (rising and falling), for which we could also use random exit velocities in a defined range for every individual particle.

[66] We observe an almost constant total echo power ($P^+ + P^-$) during secondary pulses. Both our interpretations that the volume fluxes into and out of the FOV balance until the last pulse ends, and that the net volume flux is hence zero, are not reproduced by the model. Big particles move on ballistic trajectories, but small particles move with the gas and hence are blown upwards. Therefore they still move in the FOV, when the next pulse ejects gas and new particles. Small particles accumulate in the FOV and the total echo power increases with time. Nevertheless, the attenuation of the radar beam depends on the concentration of particles, which means that at high concentration the beam does not penetrate the whole volume. This attenuation is neglected in our model. In reality, a constant total echo power can represent either a constant or an increasing volume, when the particle concentration is high enough.

[67] The main difference between synthetic and real data sets is that the most energetic events (in terms of echo power) show very high negative velocities that cannot be explained by simple ballistic motion. In principle, we were able to reproduce these velocities with several models of higher complexity. Adding turbulence to the ballistic model, for instance, broadens the region of high echo power around zero. A deviation of the directivity axis away from the radar shifts the whole velocigram toward negative velocities without changing any other pattern. A wind component away from the Doppler radar (e.g. down-slope wind) also shifts the whole velocigram toward negative velocities (see Appendix B and Figure B2). A high total echo power might also represent a high concentration, which in turn indicates that attenuation of the radar beam in the ash cloud is not negligible. Hence, we would only see the front of the cloud. In that case, the velocigram of an entrainment vortex ring will give only falling particles, because ash is dragged up in the column center (invisible to the radar) and falls down at the cloud edges (see auxiliary material for more explanation). Coupling the synthetic radar model to more accurate 3D eruption column models like ATHAM [*Oberhuber et al.*, 1998] or PDAC [*Esposti Ongaro et al.*, 2007] will enhance our understanding in future investigations. Nevertheless, the first pulse is always the same, independent of the echo power of the following pulses, whereas the second and following pulses always have a total echo power of the same order of magnitude.

[68] Although we measured comparable or even lower exit gas velocities than at Stromboli, eruption clouds at Santiaguito volcano reach heights of up to 1000–4000 m above the vent, which is one order of magnitude higher than at Stromboli. This seems indicating that buoyancy and hence the thermal potential of the erupting mixture controls the plume height rather than the gas exit velocity. However, analysis and modeling of the Doppler radar velocigrams recorded at Arenal volcano (Costa Rica) using a different Doppler radar and setting (different range gate dimensions compared to the plume, different viewing geometry) show that ballistic and ash plume dynamics can effectively be discriminated by Doppler radar and therefore be quantified separately [*Valade and Donnadieu*, 2011].

[69] In conclusion a typical eruptive event at Santiaguito seems to start with an uplift of the dome center that takes 0.5 to 1 s. No ash is visible during that time. First ash particles at higher velocities (10–15 m/s along beam) appear 1.5–2 s after the onset of uplift (i.e. ∼1 s after the uplift signal vanishes). Another 2–3 s later, a faster (20–25 m/s along beam) and more intense pulse (up to 20 dB increase) can be observed at the outer ring. This second pulse is in 83% of the observed events followed by pulses of same or less strength in terms of echo power and maximum velocity. The recurrence period of these subsequent pulses is 2–5 s with an average of 3 s.

[70] According to *Johnson et al.* [2008], the dome uplift starts in the center and migrates outwards with 30–50 m/s. Considering that the distance between the dome center and the outer ring is ∼100 m the time between center uplift and beginning of outer ring deformation is 2–3 s, which is almost identical to the time span between the first pulse (at dome center) and the second pulse (at the ring). It seems that uplift is the trigger for the eruption and initiated by a process that also mobilizes volatiles. But the volatiles need to percolate through a system of fractures in the dome before they reach the surface, which explains the time span between the onset of uplift and the first degassing (∼1.5 s).

[71] Comparing the velocigrams of the example calculations (see Figure 11) and the real data, it stands to reason that the multiple streaks observed during the eruptions are actually a sequence of single pulses. In fact such pulses have also been observed during thermal observations at Santiaguito volcano [*Sahetapy-Engel and Harris*, 2009] but their data do not reveal details on the near-vent eruption velocities. The pulsed nature of events has also been observed at other volcanoes, e.g. using infrasound at Karymsky volcano, Russia [*Lees and Bolton*, 1998; *Johnson and Lees*, 2000], photoballistics or Doppler radar at Stromboli, Italy [*Chouet et al.*, 1974; *Ripepe et al.*, 1993; *Scharff et al.*, 2008], and seismics or Doppler radar at Arenal volcano, Costa Rica [*Lesage et al.*, 2006; *Donnadieu et al.*, 2008]. At Stromboli pulses can be explained by a chain of successive bursting gas bubbles. At Karymsky, a model analogue to a pressure cooker has been proposed to explain those pulses [*Lees and Bolton*, 1998]. A somewhat similar model has been proposed by *Lesage et al.* [2006] for Arenal volcano. In their model cracks open and close rhythmically under the influence of pressure oscillations in a bubble-filled closed conduit.

[72] A possible mechanism that explains both the initial dome uplift and the occurrence of repetitive pulses during an eruptive event at Santiaguito has been proposed by *Scharff et al.* [2009] and is the focus of ongoing research. *Bluth and Rose* [2004] proposed that the magma column undergoes stick-slip motion, i.e. stepwise emergent upward displacement of the magma. Based on the model by *Johnson et al.* [2008],

we assume that below the marginal permeable dome surface uprising magma degasses increasing its gas mass fraction with height in the conduit. This magma/gas mixture becomes highly compressible due to the large amount of gas bubbles. The sudden upward motion of the magma column compresses the magma foam and triggers uplift and consecutive oscillations of the dome surface, at which in turn opening fractures give way for explosive degassing. Future work will combine our findings from the analysis of Doppler radar data with the other data sets of this multidisciplinary experiment such as infrasonic and seismic data.

## Appendix A: Doppler Radar Forward Model

[73] The Doppler radar forward model comprises two main parts: (1) the description of the movement of particles, and (2) the determination of the reflected energy from the particles moving through a hypothetical radar beam. For the dynamic part we use a Lagrangian formulation of ballistic particle transport. For every time step, every particle updates its position and velocity. A forth order Runge-Kutta algorithm is used to calculate the new velocity from the sum of forces (accelerations) acting on the particle, namely gravity and atmospheric friction. Here we assume that all particles are spheres. Following *Herzog et al.* [1998] atmospheric friction is calculated for both Newtonian and Stokian friction for each particle and the higher of both values is applied to the particle. Acceleration due to Newtonian friction depends on the drag coefficient $c_w$, the ratio of densities $\rho_g$ and $\rho_s$ (gas and solid respectively), the particle radius $r$, and the squared relative velocity $\vec{v} = \vec{v}_s - \vec{v}_g$:

$$\vec{a}_N = -c_w \frac{3\rho_g v^2}{8\rho_s r} \frac{\vec{v}}{|v|}. \tag{A1}$$

Newtonian friction typically applies to faster particles. For slower particles the acceleration due to Stokes friction is dominant because it only depends on the single relative velocity, the gas viscosity $\mu$ and the squared radius

$$\vec{a}_S = -\frac{9\mu}{2\rho_s r^2}\vec{v}. \tag{A2}$$

We calculate an isothermal atmosphere at $T = 300$ K with a density of $\rho_0 = 0.897$ kg/m$^3$ at vent elevation $z_v$ and a constant viscosity of $\mu = 1.82 \times 10^{-5}$ Ns/m$^2$. Density decreases with height $z$

$$\rho_g = \rho_0 e^{-g\frac{z - z_v}{R_{air}T}}, \tag{A3}$$

where $R_{air} = 287$ J/kg/K is the specific gas constant of air. Here we neglect density and viscosity variations with changing gas temperature, as we do not calculate the expansion and cooling of the ejected volatiles. The drag coefficient is a function of the Reynolds number, i.e. the ratio of inertial to viscous forces [see][for a review of models to calculate terminal fall velocity *Pfeiffer et al.*, 2005]. Due to our parameterization of the friction forces, we only need the drag coefficient at high Reynolds numbers (high velocities), where we follow *Pfeiffer et al.* [2005] and use $c_W = 1$ as an approximation for irregularly shaped volcanic particles.

[74] To calculate the friction terms the relative velocity between particle and gas is needed. The gas velocity is calculated at every particle position $\vec{X}_p = [x_p, y_p, z_p]$ as the superposition of background wind (constant in time and space), gas jet (see equation (A4)) and a parameterization for buoyant updraft (see equation (A5)). Note that only the background wind provides horizontal gas velocity components to the model. The gas jet is parameterized following *Dubosclard et al.* [2004] as a column of vertical wind centered at the vent with the gas speed decreasing exponentially with height [*Blackburn et al.*, 1976]. In addition the gas speed decreases radially from the maximum speed at the vent center (inspired by *Carey and Sparks* [1986]). The initial gas velocity $w_{g0}(t)$ (as a function of time), vent position $\vec{X}_v = [x_v, y_v, z_v]$ and radius $r_v$ (center and half width at half maximum of the Gaussian distribution), as well as a reference height $z_{\text{ref}}$ are prescribed. At the reference height the gas speed has decreased to 1%:

$$w_{\text{jet}}(t) = w_{g0}(t) \underbrace{e^{-4.6\frac{(z_p - z_v)}{z_{\text{ref}}}}}_{\text{vertical}} \underbrace{e^{-\frac{(x_p - x_v)^2 + (y_p - y_v)^2}{r_v^2}}}_{\text{horizontal}}. \tag{A4}$$

The thermal or buoyant updraft due to entrainment of ambient air is parameterized by an additional cylindrical column of vertical wind $w_{\text{plume}}(t)$, which is here assumed to be constant with height [*Sahetapy-Engel and Harris*, 2009]. Horizontally the updraft velocity $w_{\text{buoy}}(t)$ follows a Gaussian distribution and is a function of time (buoyancy develops due to entrainment and is not part of the initial inertia budget of the eruption):

$$w_{\text{plume}}(t) = w_{\text{buoy}}(t) e^{-\frac{(x_p - x_b)^2 - (y_p - y_b)^2}{r_b^2}}. \tag{A5}$$

Position $\vec{X}_b = [x_b, y_b, z_b]$, radius $r_b$ (center and half width at half maximum of the Gaussian distribution) and the timing of the updraft velocity are prescribed parameters. This implementation of the atmosphere distinguishes our model from the one developed by *Dubosclard et al.* [2004] and *Gouhier and Donnadieu* [2008].

[75] In our model an eruption is described as a superposition of single pulses. A pulse has the following properties: gas jet velocity evolution (maximum velocity, decay, duration), vent position, vent radius, particle size distribution (PSD, mean size, shape parameter and total volume), and opening angle, which is the maximum deviation of initial particle trajectories from the vertical. Pulses are allowed to overlap in time and/or space. Therefore we can describe scenarios of a steady one-vent eruption that endures several minutes as well as a series of short duration pulses that emanate synchronously from different vents distributed arbitrarily.

[76] After the particles new position and velocity is calculated, new particles are created at the vent and particles whose new position is below the topography are destroyed. A prescribed number of particles is created in every time step. The particles radius is selected randomly within a specified range, such that the underlying Weibull distribution is satisfied. It has been shown in previous studies that the PSD is well described by a Weibull distribution [*Weibull*, 1951; *Marzano et al.*, 2006] (see also Figure 9), which is in

turn defined by three parameters: total volume, mean particle size, and a shape parameter. Following *Chouet et al.* [1974] we assume the particle launch velocity $|v_{p0}|$ to depend on the particle radius $r$

$$\left|v_{p0}(r,t)\right| = w_{g0}(t) - \sqrt{\frac{8g\rho_s}{3c_w\rho_g}r}, \tag{A6}$$

where $w_{g0}(t)$ is equal to the gas jet velocity and varies with time according to a prescribed function (constant, linearly increasing or decreasing). The launch angle is chosen randomly within the opening angle. All particles with a negative velocity (i.e. a diameter larger than $(w_{g0}(t)/k)^2$) are removed from the calculation because they would not exit the vent.

[77] Once particle size, location, and velocity of the particles are determined from the ballistic part of the model described above, we calculate a velocity spectrum. The total back-scattered energy for each velocity sample in a range gate $P_i$ is the sum of the back-scattered energy $\sigma_j$ of each of the $N_i$ scattering particles moving in the respective distance interval at that velocity:

$$P_i = \sum_{j=1}^{N_i} \sigma_j \frac{f(\phi_j)}{R_j^4}. \tag{A7}$$

$R_j$ is the along beam distance of the particle and $f(\phi_j)$ is the beam intensity at angular distance $\phi_j$ from the beam axis. The intensity inside the synthetic radar beam follows a Gaussian distribution, which means that the intensity decreased to 50% at the half opening angle $\phi = 0.75°$. We include geometric spreading but neglect absorption, multiple scattering, and interference.

[78] Scattering of electromagnetic waves at ash particles is calculated using Mie theory [*Mie*, 1908]. In brief, Mie describes the interplay of internal and external electromagnetic fields. In the Mie region, the external field wavelength and the particle size are of the same order of magnitude. Here a so-called creeping wave [*Currie*, 1989] travels around the particle interfering constructively or destructively, hence the amount of back-scattered energy strongly depends on the ratio of particle size and wavelength. In the end-member case, when the wavelength of the external field is small compared to the particle size, the internal field will almost match the external field and the particle's back-scattering cross section is almost equal to its geometric cross section. In the Rayleigh region, when the particle is very small compared to the wavelength, the energy is scattered almost isotropically in all directions, hence only a very small fraction is back scattered toward the radar. Because we assume that size and dielectric properties do not change significantly over time, the back-scatter cross sections $\sigma_j$ need to be calculated only once for each particle size. This is done by an external program in advance. The complete description of theory and algorithm is given by *Dave* [1969] and *Toon and Ackerman* [1981].

[79] For a realistic synthetic spectrum we also account for the signal processing procedure inside the Doppler radar. Because our radar is a FMCW Doppler radar, several processing steps including two FFTs (Fast Fourier transform) are applied to the raw data to retrieve the velocity spectra [*Barrick*, 1973].

## Appendix B: The Influence of Eruption Geometry, Vent Conditions, Buoyant Updraft and Wind on the Doppler Radar Measurement

[80] This section has the purpose of giving a deeper insight into the interpretation of Doppler radar data. Using the ballistic model described above, we are able to produce velocigrams for a wide range of vent conditions and particle size distributions.

[81] In Figure B1 (left), all particles are ejected vertically ($\alpha = 0°$). In the middle and right column, the particle ejection directions follow a normal distribution with a maximum angle of $\alpha = \pm 25°$ to the vertical. As described above, the particle's initial velocity depends on its radius and a reference velocity at the vent exit (equation (3)). In Figure B1, this reference velocity is held constant at 50 m/s for 1.5 s (left and middle column) or decreases linearly from 50–10 m/s over 1.5 s. After this period, no new particles are added into the model. Particle size distribution (see Figure 9) and observation geometry (see Figure 4b) are the same in all 15 calculations shown in Figure B1.

[82] Each row in Figure B1 shows a set of velocigrams produced with identical environmental conditions in the ballistic model.

[83] 1. Frictionless: The simplest case is a particle transport without particle-air interaction (frictionless, upper row). It is clearly visible that the acceleration acting on the particles is constant and negative (simply gravity). The two maxima in echo power in the upper left velocigram (and to a smaller degree in the upper middle) show, that the initially fastest particles leave the FOV on their way up and eventually, when falling back, they enter the FOV again. However, when particles are ejected with a decreasing gas velocity (upper right), we see that most particles do not leave the FOV. This can be concluded from the maximum in echo power around zero velocity, because particles are removed from the model as they hit the ground. Thus slow or non moving particles that leave a clear signal in the velocigram are at their highest-/turning point. However, during processing of the data in the radar the zero-velocity echo power is suppressed. Ejecting particles on inclined trajectories (middle and right velocigram) leads to a wider range of measured velocities, because the radar only measures one component of the three dimensional velocity vector (see Figure 2).

[84] 2. With friction: In the second row, the particles are affected by air drag in non-moving air (i.e. no wind). Acceleration is no longer constant so that the diagonal streak gets bended toward the particles terminal settling velocity (i.e. the velocity where size dependent air drag and gravity acceleration cancel out). However, particles hit the ground and are hence removed from the model before they reach their terminal settling velocity. In the left velocigram where all particles are ejected vertically (and hence settle vertically) the high echo power around zero velocity suggests that all particles stay within the FOV. Since air drag also acts on horizontal velocity components, we can expect that no particles leave the FOV to either side even when an opening angle of 25° is considered.

[85] 3. With gas jet: The next level of complexity is the gas jet that erupts in mixture with the particles (third row in

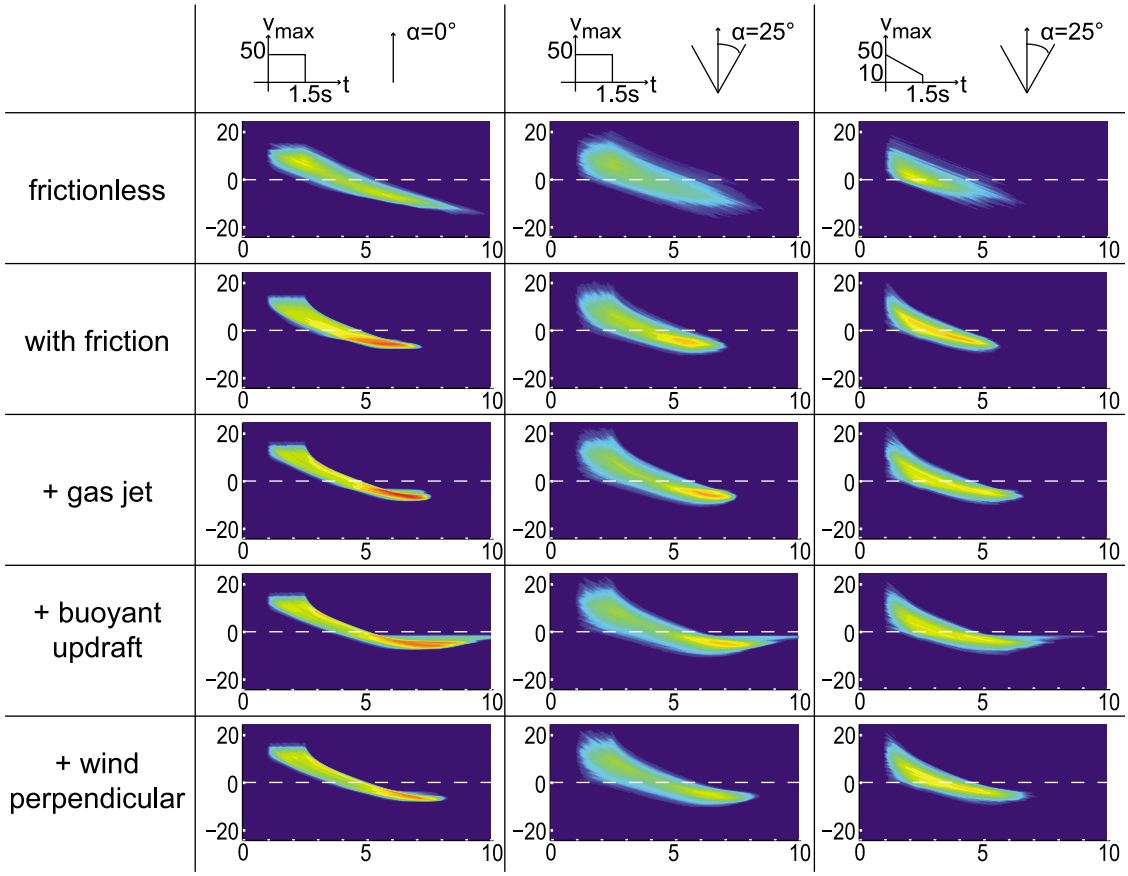


**Figure B1.** Synthetic velocigrams of 15 different parameter combinations. Varied are: opening angle and time evolution of maximum velocity (constant over columns). In each row the particle transport in the ballistic model gets more complex. The first row shows pure ballistic transport without any friction. From the second row down, friction with air is included. The third row introduces the gas jet that comes out of the vent, buoyant updraft is included in the fourth row and finally a side wind (perpendicular to radar beam) is superposed in the bottom row. The sounding geometry and PSD (see Figure 9, black line) are held constant during all calculations. Every velocigram shows the echo power (color coded) as a function of time (x-axis in seconds) and velocity (y-axis in m/s). The color bar is the same as in Figure 11. More explanation in the text.

Figure B1). Upon exiting the vent the gas behaves like a jet in the upward direction. This jet is simulated here by prescribing a vertical wind. The jet velocity equals $v_{max}$ directly at the vent, and decreases exponentially with height and lateral distance from the vent. Due to the velocity initialization all particles move with their terminal fall velocity relative to the surrounding gas. That means, inside the jet, all particles are dragged upwards with a velocity that depends on the local gas velocity and the particle radius. The smaller a particle, the faster is its absolute velocity inside the jet. Particles are dragged upwards with the jet and produce a very long coda in the velocigram when they finally fall through the FOV after the jet fades either at some pre-defined elevation (here: 50 m) or time (here: after 1.5 s). In comparison to the above 'still air'-case, some particles reach their terminal settling velocity before hitting the ground as they have been dragged to greater heights during their flight.

[86] 4. With buoyant updraft: Another key feature of ash-laden eruptions is the buoyant updraft caused by a thermal instability resulting from entrainment and heating of ambient air (herein also termed plume). Again, this updraft is implemented as a vertical wind component with a velocity of 5 m/s (constant with time and height) but laterally decaying according to a Gaussian distribution (see Appendix A). The most prominent effect in the velocigrams in row four is the long coda that consists of a broadened band of high echo power at negative velocities. Compared to the third row (no thermal plume) the maximum echo power is shifted toward positive velocities. In the left velocigram of the first four rows, all particles move vertically, i.e. they stay inside the plume. Because the particles terminal settling velocity is relative to the surrounding wind, their absolute velocity is shifted by the updraft velocity. The maximum negative velocity however equals the maximum negative velocity without plume or jet. This means again that the biggest particles (which have the largest terminal settling velocity) are not affected by air drag at all.

[87] 5. With background wind: The atmosphere is rarely at rest at a volcano. Side wind can significantly affect the velocigrams. Here (bottom row) we introduce a wind blowing at 10 m/s from right to left (perpendicular to radar beam) and explore the effects on the radar data. One can

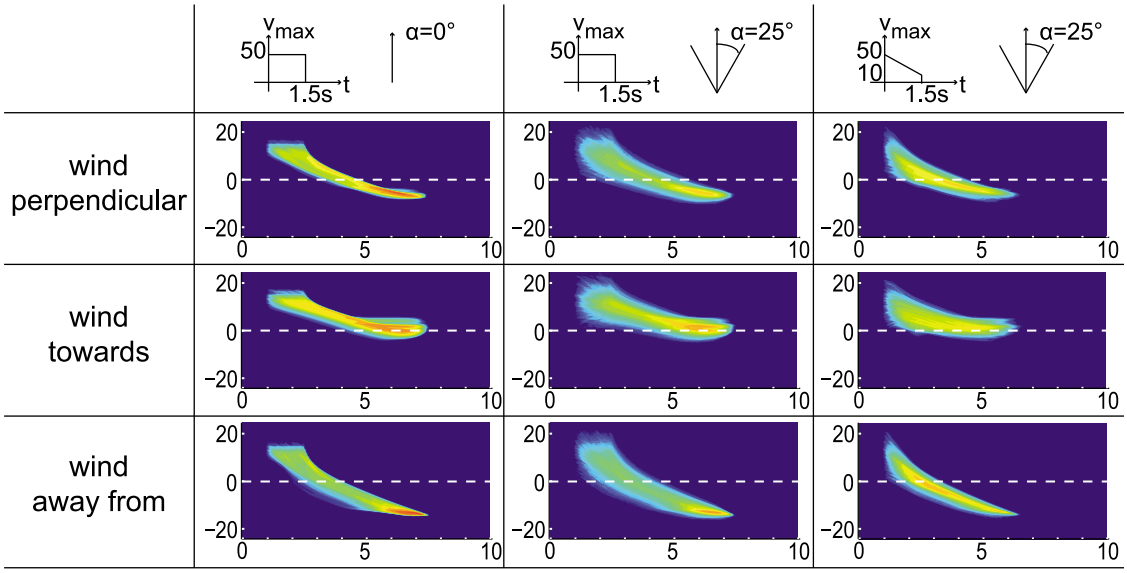


**Figure B2.** Synthetic velocigrams of 9 different parameter combinations that show the effects of wind (10 m/s). The geometry, PSD and vent conditions are the same as in Figure B1 (third row), i.e. friction with air and the gas jet are included. We neglect buoyant updraft here because the radar is pointing directly at the vent exit. We vary only the direction of the background wind (perpendicular and along the radar beam). The 'along beam'-direction is modeled separately for wind toward and away from the radar. The color bar is the same as in Figure 11. More explanation in the text.

clearly see that plume effects on the coda are strongly reduced. Particles that would rise in the plume are simply blown away and fall down as they exit the region of buoyant updraft. In the middle and right velocigram, particles that would exit the plume to the right due to their inclined ejection velocity get blown into the plume again. The main difference to the jet-simulations (third row) is that particles are carried upwards by jet and plume and sidewards by the wind so that they eventually leave the upwind region and fall down with their terminal settling velocity.

[88] One key feature of all 15 calculations is that maximum velocities are recorded only at the beginning of the events, where particles are ejected out of the vent with their highest velocity. However, ejecting particles on inclined trajectories widens the range of recorded velocities, because the radar only measures the radial velocity component. Hence the geometrical feature of non-vertically ejected particles can lead to an overestimation of the gas velocity, when inferred by vertical correction of the maximum radial velocity recorded by the radar.

[89] In Figure B2 we further explore the effects of background wind blowing from different directions (cross-beam, along-beam) at 10 m/s. Again the velocigrams are calculated for different vent conditions (see also Figure B1). In contrast to the lower row in Figure B1, we do not include buoyant updraft in these calculations. Only friction and the gas jet are used. In the upper row, wind is blowing perpendicular to the beam. The most important difference to the model without wind (Figure B1, third row, gas jet) is the lower echo power at negative velocities, some particles are simply blown out of the FOV. The middle and lower row show models with along-beam wind. Depending on the wind direction (toward or away from the radar), the later part of the velocigram (after the gas jet faded, after second 2.5 in Figure B2) is shifted to positive or negative velocities, respectively.

[90] **Acknowledgments.** Success of the field portion of this experiment was made possible with support from many people who we want to acknowledge: Raul Salguero, Rudiger Wolf, Oto Matias, Eddy Sanchez, Bill Elderbaum, Bill Rose, Richard Sanderson, Omar Marcillo, the tourist police from Panajachel, the staff at the Santiaguito Observatory, IRIS PASSCAL (providing expertise and geophysical equipment loan), and Nick Varley. Furthermore, we thank Stefan Kinne for providing insight and support for the software to calculate reflectivity coefficients. Discussions with Jörg Hasenclever and Kristina Meier regarding data interpretation were also highly appreciated. Funding for the field work of this project was provided in part by NSF EAR grant 0440225. LS was supported by a stipend of University of Hamburg and through DFG grant Ho1411 20-1. We thank M. Todesco, F. Donnadieu, and an anonymous reviewer for their thoughtful reviews, which tremendously helped to improve the manuscript. We also thank the Editor A. Revil for handling the manuscript.

## References

Adams, R. J., W. F. Perger, W. I. Rose, and A. Kostinski (1996), Measurements of the complex dielectric constant of volcanic ash from 4 to 19 GHz, *J. Geophys. Res.*, *101*(B4), 8175–8185, doi:10.1029/96JB00193.

Barmin, A., O. Melnik, and R. J. S. Sparks (2002), Periodic behavior in lava dome eruptions, *Earth Planet. Sci. Lett.*, *199*, 173–184, doi:10.1016/S0012-821X(02)00557-5.

Barrick, D. E. (1973), FM/CW radar signals and digital processing, *Tech. Rep. ERL 283-WPL 26*, Natl. Oceanic and Atmos. Admin. Environ. Res. Lab., Boulder, Colo.

Blackburn, E. A., L. Wilson, and R. S. J. Sparks (1976), Mechanisms and dynamics of Strombolian activity, *J. Geol. Soc.*, *132*, 429–440.

Bluth, J. S., and W. I. Rose (2004), Observations of eruptive activity at Santiaguito volcano, Guatemala, *J. Volcanol. Geotherm. Res.*, *136*, 297–302.

Carey, S., and R. S. J. Sparks (1986), Quantitative models of the fallout and dispersal of tephra from volcanic eruption columns, *Bull. Volcanol.*, *48*(2–3), 109–125, doi:10.1007/BF01046546.

Chouet, B., N. Hamisevicz, and T. R. McGetchin (1974), Photoballistics of volcanic jet activity at Stromboli, Italy, *J. Geophys. Res.*, *79*, 4961–4976, doi:10.1029/JB079i032p04961.

Currie, N. (Ed.) (1989), *Radar Reflectivity Measurement: Techniques and Applications*, Artech House, Norwood, Mass.

Dave, J. V. (1969), Scattering of electromagnetic radiation by a large, absorbing sphere, *IBM J. Res. Dev.*, *13*(3), 302–313.

de Michieli Vitturi, M., A. B. Clarke, A. Neri, and B. Voight (2008), Effects of conduit geometry on magma ascent dynamics in dome-forming eruptions, *Earth Planet. Sci. Lett.*, *272*, 567–578, doi:10.1016/j.epsl.2008.05.025.

Donnadieu, F., M. Gouhier, J. Fournet-Fayard, and C. Hervier (2008), Applications of pulsed ground-based Doppler radar to the study and monitoring of volcanoes, in *Proceedings of the Ground-Based Radar Observations for Volcanoes Workshop*, edited by G. Wadge and R. A. Robertson, pp. 6–8, Environ. Syst. Sci. Cent., Reading, U. K.

Dubosclard, G., R. Cordesses, P. Allard, C. Hervier, M. Coltelli, and J. Kornprobst (1999), First testing of a volcano Doppler radar (VOLDORAD) at Mount Etna, Italy, *Geophys. Res. Lett.*, *26*(22), 3389–3392, doi:10.1029/1999GL008371.

Dubosclard, G., F. Donnadieu, P. Allard, R. Cordesses, C. Hervier, M. Coltelli, E. Privitera, and J. Kornprobst (2004), Doppler radar sounding of volcanic eruption dynamics at Mount Etna, *Bull. Volcanol.*, *66*, 443–456, doi:10.1007/s00445-003-0324-8.

Esposti Ongaro, T., C. Cavazzoni, G. Erbacci, A. Neri, and M. V. Salvetti (2007), A parallel multiphase flow code for the 3D simulation of explosive volcanic eruptions, *Parallel Comput.*, *33*, 541–560, doi:10.1016/j.parco.2007.04.003.

Gerst, A. (2010), The first second of a Strombolian volcanic eruption, PhD thesis, Dep. of Geosci., Univ. of Hamburg, Hamburg, Germany.

Gerst, A., M. Hort, P. R. Kyle, and M. Vöge (2008), 4D velocity of Strombolian eruptions and man-made explosions derived from multiple Doppler radar instruments, *J. Volcanol. Geotherm. Res.*, *177*(3), 648–660, doi:10.1016/j.jvolgeores.2008.05.022.

Gonnermann, H. M., and M. Manga (2003), Explosive volcanism may not be an inevitable consequence of magma fragmentation, *Nature*, *426*, 432–435, doi:10.1038/nature02138.

Gouhier, M., and F. Donnadieu (2008), Mass estimations of ejecta from Strombolian explosions by inversion of Doppler radar measurements, *J. Geophys. Res.*, *113*, B10202, doi:10.1029/2007JB005383.

Gouhier, M., and F. Donnadieu (2011), Systematic retrieval of ejecta velocities and gas fluxes at Etna volcano using L-Band Doppler radar, *Bull. Volcanol.*, *73*(9), 1139–1145, doi:10.1007/s00445-011-0500-1.

Hale, A. J., and G. Wadge (2003), Numerical modelling of the growth dynamics of a simple silicic lava dome, *Geophys. Res. Lett.*, *30*(19), 2003, doi:10.1029/2003GL018182.

Harris, A. J. L., and M. Ripepe (2007), Synergy of multiple geophysical approaches to unravel explosive eruption conduit and source dynamics —A case study from Stromboli, *Chem. Erde Geochem.*, *67*, 1–35, doi:10.1016/j.chemer.2007.01.003.

Heliker, C., and T. N. Mattox (2003), The first two decades of the Pu'u 'Ō'ō-Kūpaianaha eruption: Chronology and selected bibliography, *U.S. Geol. Surv. Prof. Pap.*, *1676*, 1–28.

Herzog, M., H.-F. Graf, C. Textor, and J. M. Oberhuber (1998), The effect of phase changes of water on the development of volcanic plumes, *J. Volcanol. Geotherm. Res.*, *87*, 55–74.

Holland, A. S. P., I. M. Watson, J. C. Phillips, L. Caricchi, and M. P. Dalton (2011), Degassing processes during lava dome growth: Insights from Santiaguito lava dome, Guatemala, *J. Volcanol. Geotherm. Res.*, *202*, 153–166, doi:10.1016/j.jvolgeores.2011.02.004.

Hort, M., R. Seyfried, and M. Vöge (2003), Radar Doppler velocimetry of volcanic eruptions: Theoretical considerations and quantitative documentation of changes in eruptive behaviour at Stromboli Volcano, Italy, *Geophys. J. Int.*, *154*, 515–532, doi:10.1046/j.1365-246X.2003.01982.x.

Hort, M., M. Vöge, R. Seyfried, and A. Ratdomopurbo (2006), In situ observation of dome instabillities at Merapi Volcano, Indonesia: A new tool for hazard mitigation, *J. Volcanol. Geotherm. Res.*, *153*, 301–312, doi:10.1016/j.jvolgeores.2005.12.007.

Johnson, J. B., and J. M. Lees (2000), Plugs and chugs—Seismic and acoustic observations of degassing explosions at Karymsky, Russia and Sangay, Ecuador, *J. Volcanol. Geotherm. Res.*, *101*(1–2), 67–82, doi:10.1016/S0377-0273(00)00164-5.

Johnson, J. B., A. J. Harris, S. T. Sahetapy-Engel, R. Wolf, and W. I. Rose (2004), Explosion dynamics of pyroclastic eruptions at Santiaguito volcano, *Geophys. Res. Lett.*, *31*, L06610, doi:10.1029/2003GL019079.

Johnson, J. B., J. M. Lees, A. Gerst, D. Sahagian, and N. Varley (2008), Long-period earthquakes and co-eruptive dome inflation seen with particle image velocimetry, *Nature*, *456*, 377–381, doi:10.1038/nature07429.

Lees, J. M., and E. W. Bolton (1998), Pressure cookers as volcano analogues, *Eos Trans. AGU*, *79*(45), Fall Meet. Suppl., Abstract S22C-10.

Lesage, P., M. M. Mora, G. E. Alvarado, J. Pacheco, and J.-P. Métaxian (2006), Complex behaviour and source model of the tremor at Arenal volcano, Costa Rica, *J. Volcanol. Geotherm. Res.*, *157*, 49–59, doi:10.1016/j.jvolgeores.2006.03.047.

Löffler-Mang, M., M. Kunz, and W. Schmid (1999), On the performance of a low-cost K-band Doppler radar for quantitative rain measurements, *J. Atmos. Oceanic Technol.*, *16*, 379–387, doi:10.1175/1520-0426(1999)016<0379:OTPOAL>2.0.CO;2.

Marchetti, E., M. Ripepe, A. J. L. Harris, and D. D. Donne (2009), Tracing differences between vulcanian and Strombolian explosions using infrasonic and thermal radiation energy, *Earth Planet. Sci. Lett.*, *279*, 273–281, doi:10.1016/j.epsl.2009.01.004.

Marzano, F. S., S. Barbieri, G. Vulpiani, and W. I. Rose (2006), Volcanic ash cloud retrieval by ground-based microwave weather radar, *IEEE Trans. Geosci. Remote Sens.*, *44*(11), 3235–3246, doi:10.1109/TGRS.2006.879116.

Massol, H., and C. Jaupart (2009), Dynamics of magma flow near the vent: Implications for dome eruptions, *Earth Planet. Sci. Lett.*, *279*, 185–196, doi:10.1016/j.epsl.2008.12.041.

Melnik, O., and R. S. J. Sparks (2005), Controls on conduit magma flow dynamics during lava dome building eruptions, *J. Geophys. Res.*, *110*, B02209, doi:10.1029/2004JB003183.

Mie, G. (1908), Beiträge zur Optik trüber Medien, speziell kolloidaler Metallösungen, *Ann. Phys.*, *330*(3), 377–445, doi:10.1002/andp.19083300302.

Oberhuber, J. M., M. Herzog, H.-F. Graf, and K. Schwanke (1998), Volcanic plume simulation on large scales, *J. Volcanol. Geotherm. Res.*, *87*(1–4), 29–53, doi:10.1016/S0377-0273(98)00099-7.

Patrick, M. R. (2007a), Dynamics of Strombolian ash plumes from thermal video: Motion, morphology, and air entrainment, *J. Geophys. Res.*, *112*, B06202, doi:10.1029/2006JB004387.

Patrick, M. R. (2007b), The gas content and buoyancy of Strombolian ash plumes, *J. Volcanol. Geotherm. Res.*, *166*, 1–6, doi:10.1016/j.jvolgeores.2007.06.001.

Patrick, M., N. Varley, E. Ramos, A. Blankenbicker, and J. Johnson (2007), Ash plume dynamics at Santiaguito volcano, Guatemala from thermal and high resolution video, *Eos Trans. AGU*, *88*(52), Fall Meet. Suppl., Abstract V31E-0707.

Pfeiffer, T., A. Costa, and G. Macedonio (2005), A model for the numerical simulation of tephra fall deposits, *J. Volcanol. Geotherm. Res.*, *140*, 273–294, doi:10.1016/j.jvolgeores.2004.09.001.

Ripepe, M., M. Rossi, and G. Saccorotti (1993), Image processing of explosive activity at Stromboli, *J. Volcanol. Geotherm. Res.*, *54*, 335–351, doi:10.1016/0377-0273(93)90071-X.

Sahetapy-Engel, S. T., and A. J. L. Harris (2009), Thermal-image-derived dynamics of vertical ash plumes at Santiaguito volcano, Guatemala, *Bull. Volcanol.*, *71*(7), 827–830, doi:10.1007/s00445-009-0284-8.

Sahetapy-Engel, S. T. M., L. P. Flynn, A. J. L. Harris, G. J. Bluth, W. I. Rose, and O. Matias (2004), Surface temperature and spectral measurements at Santiaguito lava dome, Guatemala, *Geophys. Res. Lett.*, *31*, L19610, doi:10.1029/2004GL020683.

Scharff, L., A. Gerst, M. Hort, and J. B. Johnson (2007), The dynamics of explosions at Santiaguito volcano, Guatemala, *Eos Trans. AGU*, *88*(52), Fall Meet. Suppl., Abstract V31E-0718.

Scharff, L., M. Hort, A. J. Harris, M. Ripepe, J. Lees, and R. Seyfried (2008), Eruption dynamics of the SW crater of Stromboli volcano, Italy, *J. Volcanol. Geotherm. Res.*, *176*, 565–570, doi:10.1016/j.jvolgeores.2008.05.008.

Scharff, L., J. Hasenclever, and M. Hort (2009), Oscillating dome at Santiaguito? A simple model to explain inter-eruptive pulses, *Eos Trans. AGU*, *90*(52), Fall Meet. Suppl., Abstract V23D-2146.

Sparks, R. S. J., M. I. Bursik, S. N. Carey, J. S. Gilbert, L. S. Glaze, H. Siggurdsson, and A. W. Woods (1997), *Volcanic Plumes*, John Wiley, New York.

Steinberg, G. S., and J. I. Babenko (1978), Experimental velocity and density determination of volcanic gases during eruption, *J. Volcanol. Geotherm. Res.*, *9*(3), 89–98.

Suzuki, Y. J., T. Koyaguchi, M. Ogawa, and I. Hachisu (2005), A numerical study of turbulent mixing in eruption clouds using a three-dimensional fluid dynamics model, *J. Geophys. Res.*, *110*, B08201, doi:10.1029/2004JB003460.

Taisne, B., and C. Jaupart (2008), Magma degassing and intermittent lava dome growth, *Geophys. Res. Lett.*, *35*, L20310, doi:10.1029/2008GL035432.

Toon, O. B., and T. P. Ackerman (1981), Algorithms for the calculation of scattering by stratified spheres, *Appl. Opt.*, *20*(20), 3657–3660, doi:10.1364/AO.20.003657.

Valade, S., and F. Donnadieu (2011), Ballistics and ash plumes discriminated by Doppler radar, *Geophys. Res. Lett.*, *38*, L22301, doi:10.1029/2011GL049415.

Vöge, M., and M. Hort (2008a), Automatic classification of dome instabilities based on Doppler radar measurements at Merapi volcano, Indonesia: Part I, *Geophys. J. Int.*, *172*, 1188–1206, doi:10.1111/j.1365-246X.2007.03605.x.

Vöge, M., and M. Hort (2008b), Automatic classification of dome instabilities based on Doppler radar measurements at Merapi volcano, Indonesia: Part II, *Geophys. J. Int.*, *172*, 1207–1218, doi:10.1111/j.1365-246X.2007.03665.x.

Vöge, M., and M. Hort (2009), Installation of a Doppler radar monitoring system at Merapi Volcano, Indonesia, *IEEE Trans. Geosci. Remote Sens.*, *47*(1), 251–271, doi:10.1109/TGRS.2008.2002693.

Vöge, M., M. Hort, and R. Seyfried (2005), Monitoring volcano eruptions and lava domes with Doppler radar, *Eos Trans. AGU*, *86*(51), 537.

Voight, B., and D. Elsworth (2000), Instability and collapse of hazardous gas-pressurized lava domes, *Geophys. Res. Lett.*, *27*(1), 1–4, doi:10.1029/1999GL008389.

Weibull, W. (1951), A statistical distribution function of wide applicability, *J. Appl. Mech.*, *18*, 293–297.

Wilson, L., R. S. J. Sparks, T. C. Huang, and N. D. Watkins (1978), The control of volcanic column heights by eruption energetics and dynamics, *J. Geophys. Res.*, *83*(B4), 1829–1836.

Ziemen, F. (2008), Theoretische Betrachtungen zu Dopplerradarmessungen an Vulkanen, MSc thesis, Inst. für Geophys., Univ. Hamburg, Hamburg, Germany.

A. Gerst, European Astronaut Centre, European Space Agency, Linder Höhe, D-51147 Cologne, Germany.

M. Hort and L. Scharff, Klimacampus, Institut für Geophysik, Universität Hamburg, Bundesstr. 55, D-20146 Hamburg, Germany. (lea.scharff@zmaw.de)

J. B. Johnson, Department of Earth and Environmental Science, New Mexico Institute of Mining and Technology, 801 Leroy Pl., NM 87801, Socorro, New Mexico, USA.

F. Ziemen, Max-Planck-Institute for Meteorology, Bundesstr. 53, D-20146 Hamburg, Germany.